

# Augment Laminar Jamming Variable Stiffness Through Electroadhesion and Vacuum Actuation

Cheng Chen , Hongliang Ren , *Senior Member, IEEE*, and Hongqiang Wang , *Senior Member, IEEE*

**Abstract**—Various variable stiffness mechanisms have been developed to bestow new capabilities for the robotics community by changing the mechanical behaviors of robots. However, variable stiffness is limited in actuation, response speed, stiffness ratio, and, most importantly, modeling. This article proposes hybrid actuated laminar jamming to outperform individual actuated variable stiffness mechanisms. An analytical model for multilayer laminar jamming that accurately characterizes mechanical behaviors in experiments is first built. Comprehensive parametrical analysis based on this model serves as design guidelines for performance improvements of laminar jamming. Feedforward control further proves the validity of the proposed model and exhibits good controllability, showing response speed as fast as 5 ms. The synergy between electroadhesion and vacuum actuation significantly enhances overall performance, resulting in far greater effects than individual contributions. For instance, the proposed device generates a high stiffness that is almost impossible for individual vacuum or electroadhesion. Moreover, vacuuming increases 23% of the breakdown voltage, which leads to a larger electroadhesion force and, hence, a higher stiffness.

**Index Terms**—Hybrid actuation, laminar jamming, variable stiffness (VS).

Received 20 July 2024; revised 14 November 2024; accepted 19 November 2024. Date of publication 17 December 2024; date of current version 3 January 2025. This work was supported in part by the National Key R&D Program of China under Grant 2022YFB4701200, in part by the National Natural Science Foundation of China under Grant 52275021, in part by the Shenzhen Science and Technology Innovation Commission under Grant ZDSYS20220527171403009, in part by the Science, Technology, and Innovation Commission of Shenzhen Municipality under Grant ZDSYS20200811143601004, in part by the Southern Marine Science and Engineering Guangdong Laboratory (Guangzhou) under Grant K19313901, in part by the Key Project 2021B1515120035 (B.02.21.00101) of the Regional Joint Fund Project of the Basic and Applied Research Fund of Guangdong Province, and in part by the Hong Kong Research Grants Council (RGC) Collaborative Research Fund (CRF C4026-21G). This article was recommended for publication by Associate Editor C. Della Santina and Editor A. Menciassi upon evaluation of the reviewers' comments. (*Corresponding author: Hongqiang Wang.*)

Cheng Chen is with the Shenzhen Key Laboratory of Intelligent Robotics and Flexible Manufacturing Systems, Southern University of Science and Technology, Shenzhen 518055, China, and also with the Department of Electronic Engineering, The Chinese University of Hong Kong, Hong Kong, SAR, China (e-mail: chengchen002@cuhk.edu.hk).

Hongliang Ren is with the Department of Electronic Engineering, Shun Hing Institute of Advanced Engineering, The Chinese University of Hong Kong, Hong Kong, SAR, China (e-mail: hren@cuhk.edu.hk).

Hongqiang Wang is with the Shenzhen Key Laboratory of Intelligent Robotics and Flexible Manufacturing Systems, Southern University of Science and Technology, Shenzhen 518055, China, and also with the Peng Cheng Laboratory, Shenzhen 518066, China (e-mail: wanghq6@sustech.edu.cn).

This article has supplementary downloadable material available at <https://doi.org/10.1109/TRO.2024.3519433>, provided by the authors.

Digital Object Identifier 10.1109/TRO.2024.3519433

## I. INTRODUCTION

**S**OFT robotics have proliferated in recent decades. Unlike traditional rigid robots conducting repetitive operations precisely in well-defined scenarios, soft robots are favorable in negotiating with unpredictable environments because of their inherent compliance and deformability. On the other hand, insufficient force exertion and force transmission to the environment due to the softness become crucial drawbacks of empowering soft robots for extensive applications. Therefore, variable stiffness (VS) comes into play to address the core challenge of such compliance.

Mainstream VS mechanisms can be categorized down to (a) antagonism in structure or actuation, (b) phase transition through direct change of modulus, and (c) jamming based on material rearrangement. The actuation method also varies. Antagonistic tendon-pneumatic actuation is an early attempt to exploit longitudinal compression and radial contraction to realize stiffening [1]. Fluid-driven McKibben actuators in different bundle configurations achieve structural antagonism through simultaneous contraction and elongation [2]. However, such antagonism-based VS induces the coupling of bending motion and stiffening, which further impedes its modeling. Thermally responsive materials, such as shape memory polymers (SMPs) [3], cross three orders of magnitude of modulus from MPa to GPa. Heating circuits are required to reach the melting point in minutes [4]. Currently, only linear models are engaged [5] to describe the bending behaviors of phase transition-based VS catheters by deriving the relationship between stiffness and resistance.

The jamming mechanism is a simple yet effective approach to attain controllable VS with easily accessible materials. Jamming involves rearranging these materials through squeezing or friction generated by different actuation methods. Granular jamming adjusts the pressure gradient inside a sac pocket to present solid or fluid physical properties of particle materials sealed within the pocket. Vacuum [6] is a direct way to modulate the density of encapsulated particles. The stiffening speed can achieve rapidity within a one-second timeframe, while the devacuum process is comparatively slower due to flow rate constraints [7], [8]. Most importantly, the film material, types, shapes, and particle arrangement greatly influence the mechanical behaviors and stiffness change [9]. Therefore, the modeling is inexplicit and intricate. Recent advancements in fiber jamming involve substituting fillers with slender fibers [11]. The latest research attains 21 folds of stiffness variation

TABLE I  
COMPARISON OF EXISTING VS MECHANISM AND HALJ

Mechanism	Actuation method	Actuation value	Response time	Power consumption	Stiffness ratio	Dimension (mm)	Theoretical model	Characterization experiment
Antagonism	Tendon-pneumatic [1]	500 kPa	–	1.02 kW	0.94	23 (diameter)	–	Cantilever/lateral /axial
	Fluidic [2]	1 MPa	–	–	–10	21–29 (diameter)	FEM	Cantilever
Phase transition	Heating circuit [3]	1.4 A	10–130 s [4]	–2.4 W	120	4 (thickness)	Linear [5] and FEM	Three-point/tensile /axial
Granular jamming	Vacuum [6]	–98 kPa	0.1–60 s [7, 8]	150 W	6.3	25 (diameter)	Linear and FEM [9]	Three-point/cantilever
	Pneumatic [10]	80 kPa	–	–	6	5 (diameter)	Linear	Cantilever
Fiber jamming	Vacuum [11]	–90 kPa	–	150 W	5.6	16 (diameter)	Linear	Cantilever
	Pneumatic [12]	100 kPa	–	750 W	21.3	16 (diameter)	Slip estimation	Cantilever
Tubular jamming	Pneumatic [13]	100 kPa	–8 s	–	–4	38 (diameter)	–	Three-point
Laminar jamming	SMA [14]	0.5 A	100–150 s	5.9 W	60	7.5 (thickness)	Linear and FEM	Cantilever
	Clamp [15]	1 MPa	–	–	17	15.9 (thickness)	Linear	Cantilever
	Vacuum [16]	–101 kPa [19]	3.9 s [20]	65 W [21]	7.6	–2 (thickness)	Linear approximation [22]	Three-point
	EA [24]	2 kV	0.8 s	139 mW	7	0.8 (thickness)	Two-layer nonlinear	Three-point
	EA-ERF [30]	5 kV	<1 s	–	10–39	–5.5 (thickness)	Linear	Tensile
	Vacuum-heating circuit [31]	–101 kPa and 2 A	16–357 s	46 W (heating)	15.7	2.3 (thickness)	FEM	Three-point
	<b>*EA-vacuum</b>	<b>–80 kPa and 3 kV</b>	<b>5 ms–7.6 s</b>	<b>0.14–150 W</b>	<b>75.5</b>	<b>0.9 (thickness)</b>	<b>Multilayer nonlinear</b>	<b>Three-point</b>

\* indicates this work.

and builds a complete mechanical model by estimating the slip thresholds between fibers [12]. However, large discrepancies still exist between theoretical and experimental results. Instead of vacuuming, tubular jamming utilizes hollow tubes as jamming fillers by inflating against each other [13]. It is bulky in volume, and no model has been available so far.

Among jamming mechanisms, laminar jamming emerges as a highly favorable mechanism due to its advantageous attributes, such as lightweight composition and substantial VS ratio. By stacking planar materials into a layered structure, laminar jamming realizes VS via actively adjusting the coupling degree between these layers. Layers become fully jammed for a strong couple force and, therefore, effectively enlarge the equivalent moment of inertia to be stiffened when resisting a large external force until overcoming the interlayer coupling, i.e., the friction force. The interlayer friction force and the number of stacked layers regulate its mechanical behaviors and stiffness variations. Different actuation methods that generate the friction force, such as shape memory alloy (SMA) and clamps [14], [15], are applicable. However, the structure is discretized into finite elements and is not uniformly pressurized, so the mechanical model is complicated. Vacuum actuation [16], [17], [18] is proposed to realize uniform interlayer attachment. However, it is limited by the atmospheric pressure [19] (–101 kPa), and the response is slow in seconds [20], both restricting its mechanical performance. Another actuation strategy to provide such interlayer friction, electroadhesion (EA), is favored for

low energy consumption in milliwatts and short response time in milliseconds [24] due to the small leakage current and the fast charging/discharging process, respectively. Electrode films [24], [25] and dielectric elastomers [26] as jamming layers realize layers coupling through electroadhesive pressure but are restricted by the breakdown voltage of dielectric materials. Besides bending/flexural stiffness, EA clutch [27] achieves a large range of softness sensations for haptic applications by controlling the EA force in the shear direction. Efforts have been made to enhance the EA force by chemically depositing ultrathin Parylene [28] as the dielectric material or screen coating Luxprint [29] with P(VDF-TrFE-CTFE) of a high dielectric constant.

To further enhance the stiffness/force performance, hybrid laminar jamming is proposed by integrating different VS strategies. EA-actuated laminar jamming fills interlayer gaps with electrorheological fluid (ERF) [30] as dielectric, utilizing its high permittivity and rheological effect to achieve 10 times tensile force. SMP as jamming layers [31], hybrid vacuum-heating laminar jamming fulfills 15.7 times stiffness variation. However, the mutual influences behind the hybrid mechanisms remain to be investigated. For most jamming devices in Table I, although standard cantilever/three-point bending tests are conducted to experimentally characterize the stiffness, few theoretical models successfully explain such stiffness variation. Linear models [14], [15] fail to predict nonlinear mechanical behaviors. Efforts have been made to estimate nonlinear

TABLE II  
NOMENCLATURE AND DEFINITIONS

Symbol	Unit	Definition
$\epsilon_0$	F/m	Vacuum permittivity constant
$\epsilon_r$	-	Relative permittivity constant of dielectric
$d/d_a$	$\mu\text{m}$	Dielectric/air gap thickness
$U$	kV	Applied voltage on electrodes
$U_b$	kV	Maximum breakdown voltage on electrodes
$P_{EA}/P_V/P$	kPa	Electroadhesive/vacuum/hybrid pressure
$\mu$	-	Frictional coefficient between electrode films
$h_c/h_e/h_c$	$\mu\text{m}$	Encapsulation/electrode film/equivalent layer thickness
$E_t/E_e/E_c/E_T$	GPa	Plane strain modulus of encapsulation/electrode film/equivalent layer/transformed layer
$b/b_e/b_c$	mm	Width of electrode film/transformed electrode film/transformed equivalent layer
$L$	mm	Length of electrode
$A$	$\text{mm}^2$	Effective EA area between electrode films
$I_e/I_c$	$\text{mm}^4$	Moment of inertia of electrode film/equivalent layer
$A_e/A_c$	$\text{mm}^2$	Cross-section area of electrode film/equivalent layer
$l$	mm	Support span
$n$	-	Number of counted stacked layers of HALJ
$K_{U(n)}/K_{J(n)}$	mN/mm	Unjamming/jamming stiffness of an $n$ -layer HALJ
$R_{(n)}$	-	Stiffness ratio of an $n$ -layer HALJ
$F$	mN	External force applied at the midspan of HALJ
$w$	mm	Corresponding deflection at the midspan under $F$
$F_{C(n,1 \text{ to } n)}$	mN	Yield force for an $n$ -layer HALJ at yield point 1 to $n$
$w_{C(n,1 \text{ to } n)}$	mm	Corresponding deflection at yield point 1 to $n$
$\tau_{MAX}$	kPa	Maximum shear stress at the contacting interface of two-layer HALJ
$S$	$\mu\text{m}$	Variable distance between NA and Centroid of two-layer HALJ
$NA(w)$	-	Normalized variable distance of $S$
$S_i$	$\mu\text{m}$	Variable distance between $NA_i$ and Centroid $i$ of the $i$ th layer of the top half $n$ -layer HALJ
$NA_i(w)$	-	Normalized distance of $S_i$
$K_i$	mN/mm	Jamming stiffness constant from the $i$ th layer
$k_c$	-	Correction coefficient of $K_1$
$S_{z1 \text{ to } z2}$	$\text{mm}^3$	First moment of cross-section above Interface I/II with respect to the corresponding NA
$I_{J(4,1 \text{ to } 2)}$	$\text{mm}^4$	Moment of inertia at yield point 1/2 for four-layer HALJ
$\tau_{MAX,1 \text{ to } 2}$	kPa	Maximum shear stress at Interface I/II of four-layer HALJ
$B_2/B_4$	-	Proximity of the two/four-layer HALJ between fully sliding state and unjammed state
$C_{(n,i)}$	-	Analytical solutions of $NA_i(w)$
$A_{(n,3i-2 \text{ to } 3i)}$	-	Analytical solutions of $NA_i(w)$
$S(K_J^{(n)}, l/h_e/n)$	-	Sensitivity of $l/h_e/n$ with respect to $K_J^{(n)}$
$C$	nF	Capacitance of two-layer HALJ
$I$	$\mu\text{A}$	Leakage current of two-layer HALJ under $U$
$Q$	$\mu\text{C}$	Accumulated electrical charges of two-layer HALJ under $I$
$m/c/k$	-	Mass/damping/spring constant parameters of the air gap second-order system
$\Delta d_a$	$\mu\text{m}$	Air gap change output in the second-order system
$\Delta P$	kPa	Pressure inside vacuum envelope
$B/K$	-	Air-related constant parameters of Pashen's law

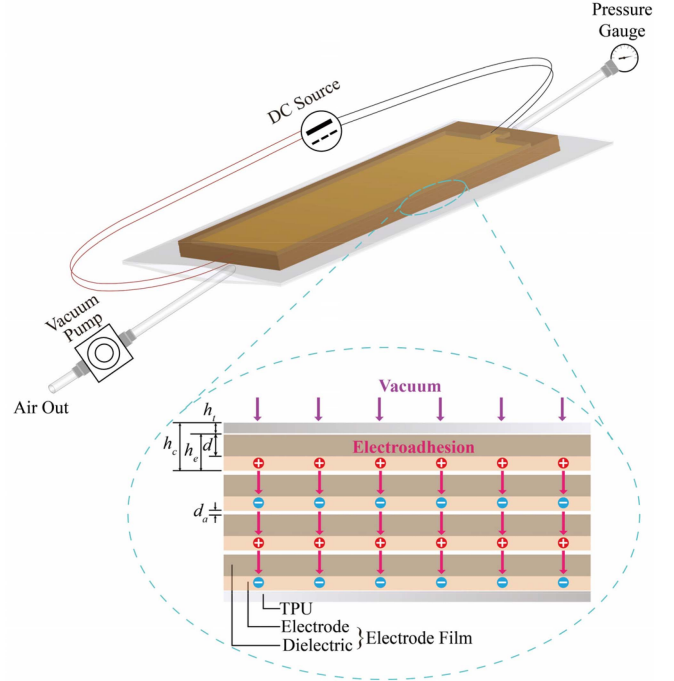


Fig. 1. Schematic of the four-layer HALJ under hybrid actuation of EA and vacuum for VS augment. The enlarged inset illustrates layer composition of HALJ.

variation through linear approximation, but as errors build up, discrepancies with both finite element methods (FEM) [22] and experimental tests [23] still exist in large deformation. Though a nonlinear jamming model presents high accuracy with experiments [24], it only applies to a simple situation—two homogeneous layers. Therefore, a more extensive model that fits a generalized form-heterogeneous  $n$ -layer structure remains to be built, considering encapsulation, which is usually neglected under vacuum actuation [16], [22], [31], also plays a role in jamming.

With the hybrid laminar jamming concept being suggested, this work proposes hybrid actuated laminar jamming (HALJ, Fig. 1) of EA-vacuum combination to outperform individual actuated VS. A nonlinear theoretical model for a multilayer jamming structure is first built by introducing influences of encapsulation and electrode films, then is experimentally validated with high accuracy. Feedforward control shows good controllability of the model and a fast response speed of 5 ms. Due to the EA-vacuum synergy, HALJ successfully surpasses the 101 kPa atmospheric pressure limitation for vacuum-based [19] and increases 23% of the breakdown voltage for EA-actuated [24].

The rest of this article is organized as follows. The fabrication process is detailed in Section II. Section III builds a multilayer model with analytical solutions by considering the influences of encapsulation and electrode films on mechanical behaviors and stiffness variation. A model-based quantitative parametrical

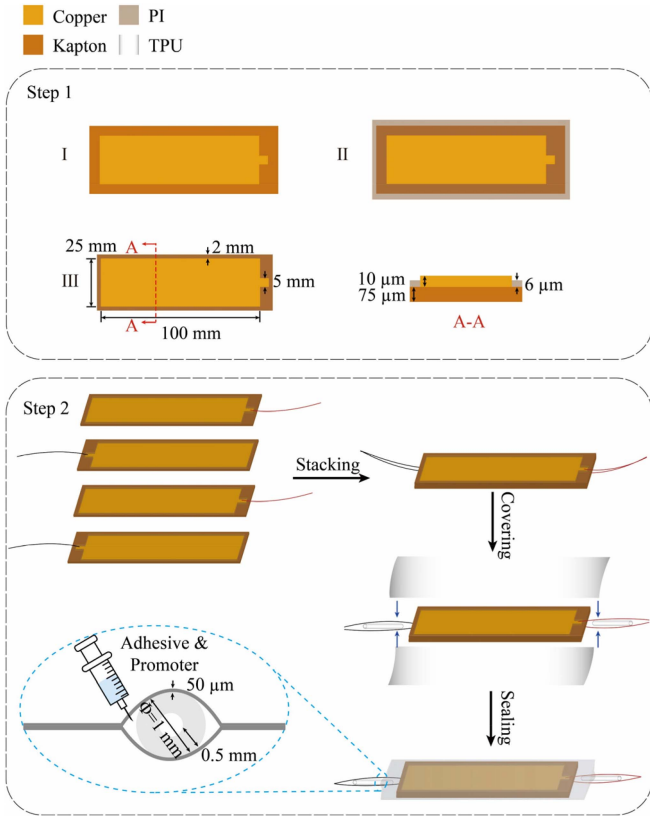


Fig. 2. Fabrication process of a four-layer HALJ, including the electrode film, wiring, tubing, and the final encapsulation.

analysis is also given in this section as design guidelines for laminar jamming to improve performances. Section IV shows high agreement between experimental results and theoretical predictions of HALJ under individual/hybrid actuation. The mutual influences of coupled electrical and negative pressure fields are experimentally characterized for hybrid actuation. Finally, Section V concludes this work and discusses suggested future work.

## II. MATERIALS AND FABRICATION

HALJ requires electrodes and dielectrics for interlayer EA generation and an airtight envelope for vacuum environments. The fabrication and assembly process of wired electrode films and a tubed encapsulation chamber are detailed in the following.

### A. Electrode Film

An electrode film is composed of a layer of ultrathin copper foil as the electrode and a layer of polyimide (PI) as the dielectric. First, a cropped 100 mm × 25 mm copper foil (10 μm, Shengze Metal Material) with an extra 5 mm × 5 mm strip for external wiring was adhered to a Kapton tape substrate (75 μm, DuPont). Then, a 2 mm wide PI (6 μm, DuPont) frame covered the copper foil surroundings to prevent edge breakdown. Finally, the electrode film forms a planar rectangular shape. The fabrication process, dimensional details, and section view of the electrode film are shown in step one of Fig. 2.

### B. Encapsulation

As illustrated in Fig. 2, step two, four identical electrode films were loosely stacked together, following a classic cathode-anode staggered arrangement where electrode films at the same electric potential are wired out (36 AWG, Triumph Cable) at the same end, avoiding voltage breakdown due to wire interferences. Two 0.5 mm × 1.5 mm TPU tubes were prepared at both ends of the four-layer structure for vacuum tubing. At last, TPU films (50 μm, Jinda Plastic) formed an airtight envelope from the top and bottom to encapsulate tubes and the layered structure through a hand clamp sealer (IPS 600, Yingke Package). Air gaps between the tubes and envelope were filled with an instant adhesive and promoter combo (406 and 770, Loctite) for better sealing. A four-layer HALJ weighs 2.8 g (tubing and wiring excluded) and measures 139 mm × 39 mm × 440 μm.

## III. MODELING

The HALJ model of two layers is built based on the previous work [24], then is extended to four layers, followed by a more general situation of  $n$  heterogeneous layers where the encapsulation influences of thickness and modulus on stiffness ratio, force performance, and sliding behaviors are considered. The theoretical model explains the augment mechanism of hybrid actuation and determines the sliding sequence by calculating shear stresses at all contacting interfaces. After that, analytical solutions of neutral axes (NA) movement that yield to boundary conditions successfully depict all mechanical behaviors of HALJ under three-point bending tests. This model exhibits sufficient rigor to align with the experimental results, whether under individual voltage driving, pure vacuum, or hybrid actuation, and successfully tracks target stiffness signals.

### A. Two Layers

A two-layer HALJ is composed of two electrode films and two layers of TPU film encapsulating them. The electroadhesive pressure between electrode films is calculated as follows:

$$P_{EA} = \frac{1}{\varepsilon_0 \left( \frac{d_a}{\varepsilon_0} + \frac{d}{\varepsilon_0 \varepsilon_r} \right)^2} \frac{U^2}{2} \quad (1)$$

where  $U$  is the voltage applied on electrode films,  $\varepsilon_0$  is the vacuum permittivity constant,  $\varepsilon_r$  and  $d$  are the relative permittivity constant and thickness of dielectric material, respectively, and  $d_a$  is the air gap between electrode films. Besides, the negative pressure gradient  $P_V$  from direct vacuuming also contributes to jamming

$$P = P_{EA} + P_V. \quad (2)$$

The top half structure, namely, a layer of TPU film and an electrode film, is considered a composite. The equivalent plane strain modulus of the composite layer is calculated as follows:

$$E_c = E_e \frac{h_e}{h_e + h_t} + E_t \frac{h_t}{h_e + h_t} \quad (3)$$

where  $E_t$  and  $h_t$  are the plane strain modulus and thickness of TPU, and  $E_e$  and  $h_e$  are the plane strain modulus and thickness of

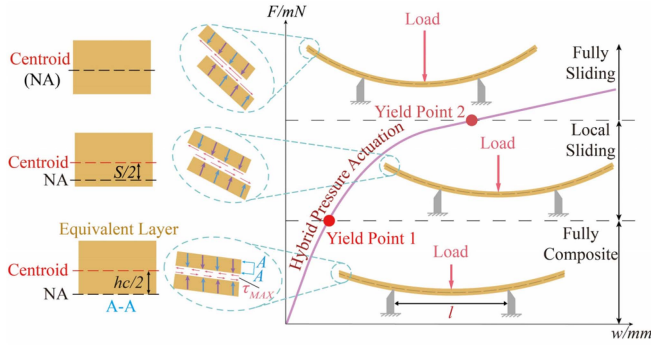


Fig. 3. Schematic of mechanical behaviors for a two-layer HALJ under a three-point bending test. HALJ maintains a high stiffness where NA remains still at the interface at the beginning of bending. When the shear stress overcomes the friction force (yield point 1), NA starts to move to the Centroid. Once NA coincides with the Centroid, HALJ reaches its lowest stiffness, indicating the fully sliding regime commencement.

the electrode film. Accordingly, the unjamming stiffness  $K_{U(2)}$  equals the stiffness summation of two equivalent layers

$$K_{U(2)} = 2 \frac{48E_c I_c}{l^3} = 2 \frac{48E_c b h_c^3}{l^3} \quad (4)$$

where  $l$  is the support span in three-point bending (the right of Fig. 3),  $h_c = h_e + h_t$ ,  $b$ , and  $I_c$  are the thickness, width, and moment of inertia of the equivalent layer. Once actuated, the jamming stiffness is contributed by the unjamming stiffness and the jamming component from two equivalent layers with respect to the contacting interface

$$K_{J(2)} = K_{U(2)} + 2 \frac{48E_c A_c}{l^3} \left( \frac{h_c}{2} \right)^2 \quad (5)$$

where  $A_c = b h_c$  is the cross-section area of the equivalent layer. Interlayer sliding between electrode film and TPU is not considered as they are composite. Therefore, the to-be-analyzed contacting interface correspondingly reduces to one.

The maximum shear stress along this interface is derived as follows:

$$\tau_{MAX} = \frac{3F_{C(2,1)}}{8b h_c} = \mu P. \quad (6)$$

$F_{C(2,1)}$  is the critical external force to overcome the interlayer friction force, defining yield point 1 to distinguish the linear region where layers are considered fully jammed and the non-linear region where interlayer sliding happens. By following the governing equation [24]

$$F(w) = K_{U(2)} w (1 + 3NA(w)^2) \quad (7)$$

where

$$NA(w) = \frac{S/2}{h_c/2} = C_{(2)} + A_{(2,1)} w^{-3/2} + A_{(2,2)} w^{-1/2} + A_{(2,3)} w^{1/2} \quad (8)$$

is the normalized distance between NA and Centroid, as shown on the left of Fig. 3.  $C_{(2)}$  and  $A_{(2,1-3)}$  are undetermined coefficients. By defining stiffness  $K(w)$  as the first-order derivative of (7), the second term in (5) decreases with variable  $S$  due to

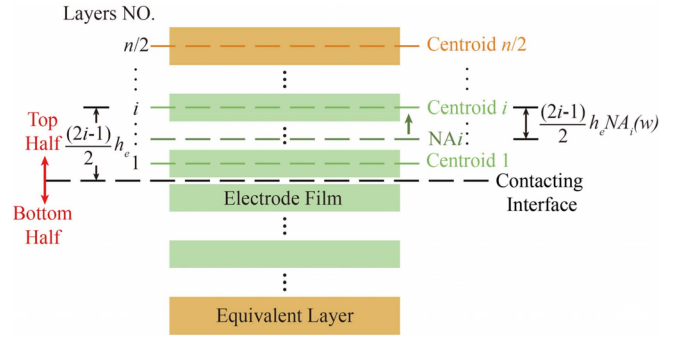


Fig. 4. NA movement illustration of the  $i$ th layer for  $n$ -layer HALJ jamming model.

such NA movement. Forces and stiffnesses continuities should yield to the boundary conditions at yield points 1 and 2

$$\begin{cases} F(w_{C(2,1)}) = K_{J(2)} w_{C(2,1)} = F_{C(2,1)} \\ F(w_{C(2,2)}) = F_{C(2,2)} \\ K(w_{C(2,1)}) = K_{J(2)} \\ K(w_{C(2,2)}) = B_2 K_{U(2)} \end{cases} \quad (9)$$

where  $B_2$  denotes the proximity of the two-layer HALJ in the fully sliding state to that in its unjammed state. The work done by the external load during the local sliding regime equals that in the corresponding regime of the unjammed state

$$\begin{cases} \int_{w_{C(2,1)}}^{w_{C(2,2)}} F(w) dw = \frac{(F_{C(2,2)} - F_{C(2,1)})^2}{2K_{U(2)}} \\ F_{C(2,2)} = \frac{B_2 F_{C(2,1)}}{B_2 - 1} \end{cases} \quad (10)$$

The detailed derivations for four-layer HALJ are in the Appendix. Theoretical solutions and results for two and four layers are in Section IV.

## B. Multiple Layers

Since EA actuation requires pairs of electrodes for external voltage, the unjamming stiffness  $K_{U(n)}$  for HALJ with an arbitrarily even number of layers  $n$  equals the sum of the stiffnesses of two equivalent layers and  $(n-2)$  electrode films

$$K_{U(n)} = (n-2) \frac{48E_e I_e}{l^3} + 2 \frac{48E_c I_c}{l^3}. \quad (11)$$

The jamming stiffness  $K_{J(n)}$  should consider the unjamming stiffness for all included layers and the jamming component for each layer with respect to the contacting interface at the central axis

$$K_{J(n)} = K_{U(n)} + 2 \frac{48E_e A_e}{l^3} \left( \frac{h_e}{2} \right)^2 + \dots + 2 \frac{48E_e A_e}{l^3} \left( \frac{(2i-1)h_e}{2} \right)^2 + \dots + 2 \frac{48E_e A_e}{l^3} \left( \frac{(n-1)h_e}{2} \right)^2 \quad (12)$$

where  $h_e(2i-1)/2$  indicates the distance between  $NA_i$  and Centroid  $i$  of the  $i$ th layer of the upper half structure when  $NA_i$  maintains at the interface before sliding, as shown in Fig. 4. The constant before  $48E_e A_e/l^3$  in (12) includes the jamming

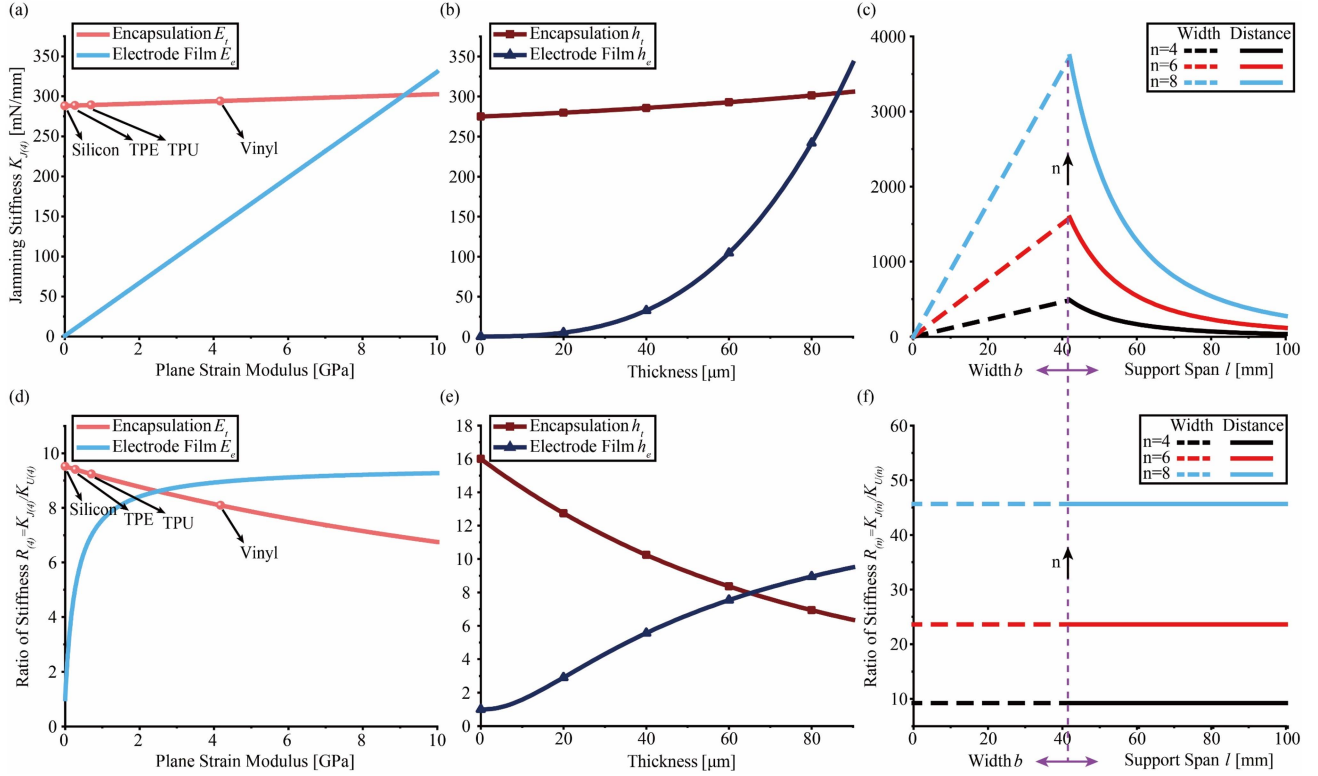


Fig. 5. Parametrical analysis of stiffness-related performance of HALJ in terms of materials and dimensions. The effect of (a) plane strain moduli, (b) thicknesses of electrode films and encapsulating materials, (c) width, support span, and number of layers of HALJ on jamming stiffness, and (d) and (e) corresponding stiffness ratio in the fully composite regime are analyzed. Different commercialized materials are illustrated. If not explicitly stated, other parameters remain the same as the fabricated four-layer HALJ of this study.

component from the bottom half structure. Therefore, the corresponding ratio of stiffness is

$$R_{(n)} = \frac{K_{J(n)}}{K_{U(n)}} = 1 + \frac{48E_e J_e}{l^3} \frac{n(n-1)(n+1)}{K_{U(n)}}. \quad (13)$$

Noted that without considering the encapsulation influence in (11), (13) degrades into  $R_{(n)} = n^2$ , conforming to the previous simplified model [16]. For instance, a ten-layer jammed HALJ is 75.5 times stiffer than that in the unjammed state, rather than 100 times, causing a 32.5% deviation due to encapsulation, which explains the stiffness ratio loss for vacuum-based laminar jamming.

As shown in Fig. 4, by introducing NA movement of an arbitrary layer of the top half and considering the same NA trajectory of the symmetrical layer at the bottom half during sliding, the governing equation is as follows:

$$F(w) = K_{U(n)}w + K_1 N A_1^2(w)w + \dots + K_i N A_i^2(w)w + \dots + K_{n/2} N A_{n/2}^2(w)w \quad (14)$$

where  $K_i$  is the  $i$ th term in (12), and

$$N A_i(w) = \frac{S_i/2}{(2i-1)h_e/2} = C_{(n,i)} + A_{(n,3i-2)}w^{-3/2} + A_{(n,3i-1)}w^{-1/2} + A_{(n,3i)}w^{1/2} \quad (15)$$

is the corresponding normalized distance. The stiffness follows the same definition as (A10) for four layers. For an  $n$ -layer HALJ, there are  $n$  yield points accordingly. Hence, forces and stiffnesses continuities should satisfy the boundary conditions at those yield points, and the form of works in the  $(n-1)$  transition stages follow similar relationships as (A16). To determine the yield points, the sliding behavior at each contacting interface, i.e., the NA movement sequence, should be analyzed. Taking four layers as an example, sliding happens from the outer to central layers because of encapsulation existence, not as the previous model assumes [22], [23]. The theoretical force deviation for different sliding assumptions can be up to 290% (see the Appendix). Once the sliding sequence is settled, the mechanical behaviors at any regime can be determined by solving NA movements of all layers. The detailed modeling framework for two-layer and four-layer HALJ is in S1. All related symbols and their definitions for the modeling are listed in Table II.

### C. Parametrical Analysis

Here, design optimization for performance improvement is given based on the previously built multilayer model regarding materials, geometry, and actuation. Fig. 5 exhibits the influences of moduli and dimensionalities of HALJ on stiffness-related performance in the fully composite regime. Since HALJ is composed of electrode films and encapsulation, Fig. 5(a) and

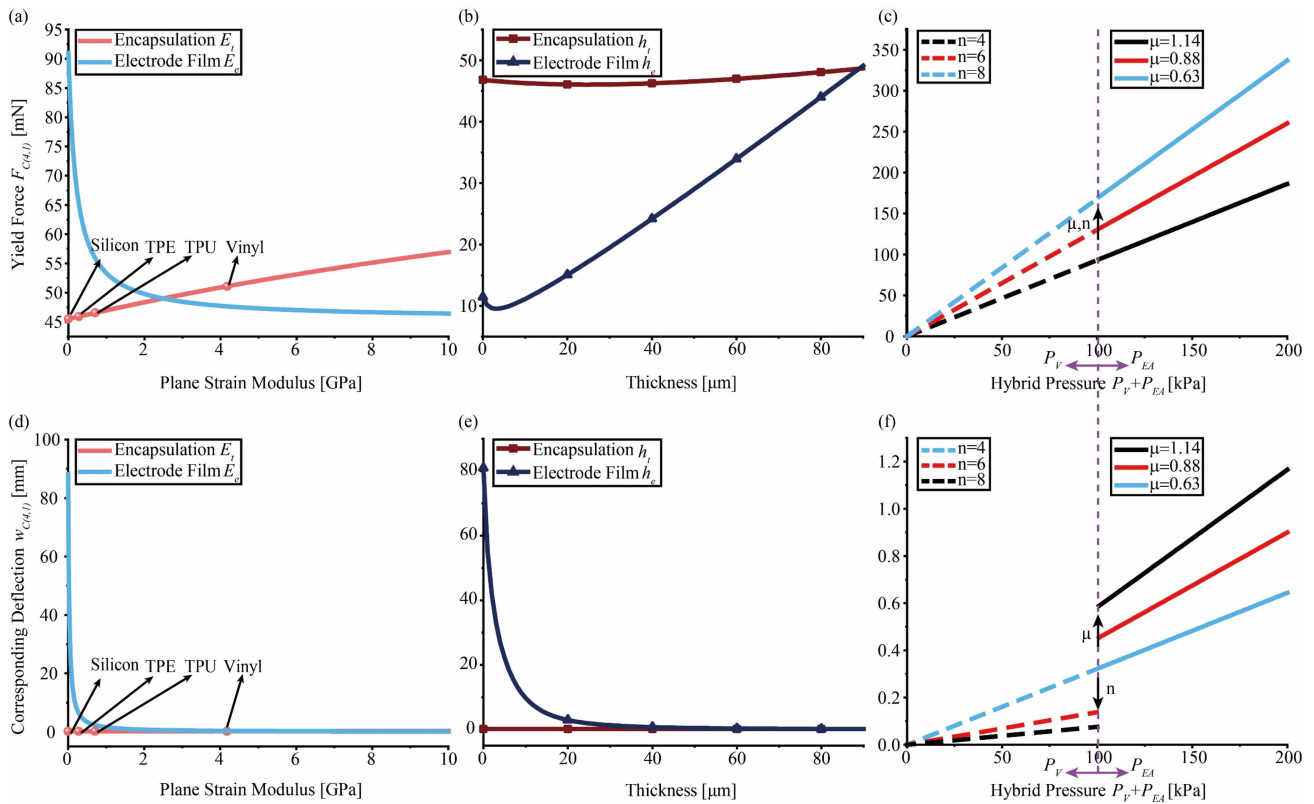


Fig. 6. Parametrical analysis of the force-related performance of HALJ in terms of materials, dimensions, and actuation. The effect of (a) plane strain moduli, (b) thicknesses of electrode films and encapsulating materials, (c) number of layers, coefficient of friction, and actuation pressure of HALJ on the critical force at yield point 1, and (d)–(f) corresponding deflection are analyzed. Different commercialized materials are illustrated. If not explicitly stated, other parameters remain the same as the fabricated four-layer HALJ of this study.

(b) present that the jamming stiffness largely increases with both the plane strain modulus  $E_e$  and the thickness  $h_e$  of electrode films, while the plane strain modulus  $E_t$  and the thickness  $h_t$  of encapsulation have a much smaller impact. Four common commercial encapsulating materials, silicon (eco-flex), TPE, TPU (this work), and vinyl, are given as examples. Regarding dimensions, the jamming stiffness gradually increases with the width  $b$  of electrode films but drastically drops with the support span  $l$  in Fig. 5(c). The number of layers  $n$  also significantly impacts the jamming stiffness. In terms of stiffness ratio, it rises for the plane strain modulus and the thickness of electrode films [Fig. 5(d) and (e)]. As the jamming layers, the electrode film considerably affects the stiffness ratio by minimizing it to the value of 1 when  $h_e = 0$ . On the contrary, the stiffness ratio decreases with the increase of plane strain modulus and the thickness of encapsulation. Especially when encapsulation is removed ( $h_t = 0$ ), the stiffness ratio reaches its maximum value of 16 for a four-layer HALJ [Fig. 5(e)]. Both width and support span show no influence, while the number of layers greatly affects the stiffness ratio, as depicted in Fig. 5(f).

Regarding force-related performance, as exhibited in Fig. 6(a), the critical force  $F_{C(4,1)}$  of four-layer HALJ at yield point 1 steadily rises for the plane strain modulus of encapsulation and sharply drops for electrode films. Fig. 6(b)

reveals an interesting relationship between thicknesses and critical forces. The critical force experiences a small U-turn for the encapsulation thickness and a large one for electrode films (initially decrease followed by an increase). Moreover, whether under individual or hybrid actuation, the critical force linearly increases with the actuation pressure [Fig. 6(c)]. The number of layers and coefficient of friction  $\mu$  also enhance the critical force. Regarding the corresponding deflection  $w_{C(4,1)}$  at yield point 1, it decreases with the plane strain modulus and thickness of electrode films accordingly but is barely affected by encapsulation, as shown in Fig. 6(d) and (e). Although the actuation pressure still conforms to a linear relationship with the corresponding deflection, unlike Fig. 6(c), the number of layers and the coefficient of friction present an opposite trend on deflection [Fig. 6(f)].

The HALJ performance in nonlinear regimes is also analyzed in Fig. 7. The green lines in Fig. 7(a) and (b) represent the reference value of 1 for HALJ in the unjammed state. The stiffness ratio starts from its maximum value of 9.24 for a four-layer HALJ under any actuation. It initially remains at its highest, followed by a decrease after the first sliding happens, approaching the reference line as the deflection increases. Though the change in the width of electrode films does not impact the linear regime, it affects nonlinear mechanical behaviors. The reason is that width influences both the jamming stiffness, as shown in Fig. 5(c),

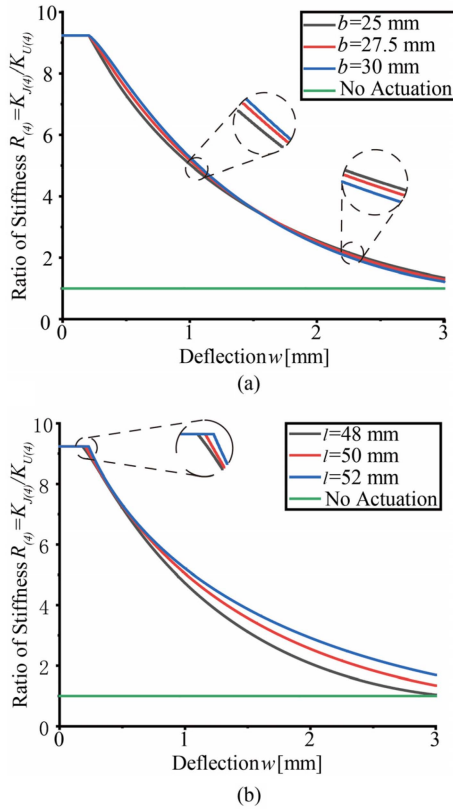


Fig. 7. Bending performance of HALJ. The influences of (a) width of the electrode film and (b) support span on the stiffness ratio through the entire bending process, encompassing both linear and nonlinear behaviors, are exhibited. If not explicitly stated, other parameters remain the same as the fabricated four-layer HALJ of this study.

and the critical force through the shear stresses in (A5), which are determined by the transformed widths described in (A4). Therefore, HALJ with a larger width shows a slower stiffness variation before the deflection of approximately 1.5 mm and then becomes faster after that [Fig. 7(a), enlarged insets]. A larger support span  $l$  shows a small increase in the corresponding deflection at yield point 1, prolonging the linear regime [Fig. 7(b), enlarged inset], but unlike the width, it consistently exhibits a slower stiffness ratio variation before reaching the reference line.

#### D. Design Guideline and Sensitivity Analysis

After comprehensive investigations of such parametrical analysis, the design guideline for laminar jamming with multi-parameter inputs extends beyond two layers for performance improvements. HALJ with high jamming stiffness and a large stiffness ratio can be achieved by increasing the electrode film modulus and replacing the encapsulation with a lower modulus and thickness. However, the yield force and the corresponding deflection decrease accordingly. Another approach, though the corresponding deflection of the linear regime is still sacrificed, is increasing the thickness of electrode films to maintain a high jamming stiffness and a large stiffness ratio simultaneously. To compensate for the sacrificed linear regime, a direct solution is

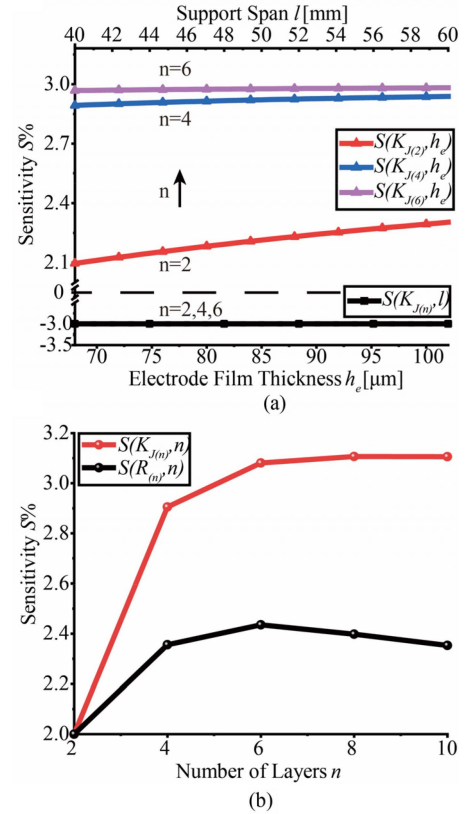


Fig. 8. Sensitivity analysis of (a) support span and electrode film thickness with respect to the jamming stiffness for HALJ with different number of layers, and (b) number of layers with respect to the jamming stiffness and stiffness ratio. If not explicitly stated, other parameters remain the same as the fabricated four-layer HALJ of this study.

increasing the interlayer friction force, that is, applying a larger actuation pressure. However, the vacuum pressure is limited by the external pump source and the atmospheric pressure (101 kPa maximum), and the electroadhesive pressure is significantly determined by the electrical properties of the insulation material used in electrode films. Besides investigating and discussing different design inputs, sensitivity analysis is conducted to quantify and evaluate the effect of parametrical changes on the stiffness-related output. To compare the influences for different parameters, the sensitivity, taken support span with respect to the jamming stiffness as an example, is defined as follows:

$$S(K_{J(n)}, l) = \frac{\partial K_{J(n)}}{\partial l} \frac{l}{K_{J(n)}} \quad (16)$$

which means a 1% increase in  $l$  results in a  $S\%$  increase in  $K_{J(n)}$ . All parameters involved in this model are investigated, some of which cause the value of sensitivity  $S$  to be larger than two are selected and considered sensitive. As shown in Fig. 8(a),  $S(K_{J(n)}, l)$  remains constant at the value of  $-3$  regardless of the number of layers, while  $S(K_{J(n)}, h_e)$  increases with both electrode film thickness and the number of layers but is smaller than 3. In total,  $\pm 20\%$  variation range is applied for all investigated parameters. Fig. 8(b) illustrates that the jamming stiffness is more sensitive than the stiffness ratio to the number of layers.

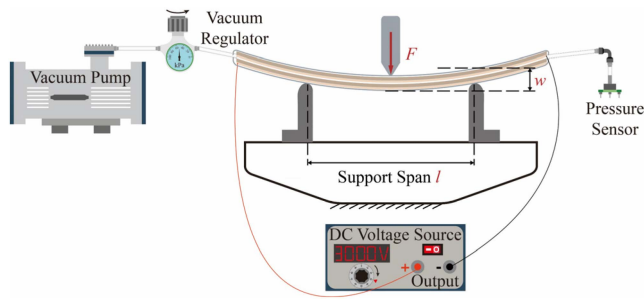


Fig. 9. Experimental setup of the three-point bending for HALJ under hybrid actuation.

Therefore, besides materials and actuation, the dimensionalities that exhibit significant impacts on stiffness should be carefully considered in design and fabrication.

Finally, the final HALJ prototype design can be decided based on the parametrical analysis and fabrication process. Kapton tape as the dielectric is a commercially available and low-cost material with stable electrical properties. In total,  $75\ \mu\text{m}$  thickness can withstand up to 5 kV, providing a wide range of driving voltages. In total,  $10\ \mu\text{m}$  copper film as an electrode reduces the unjamming stiffness since it largely determines the electrode film modulus. In contrast, thicker coppers sacrifice flexibility, while thinner ones easily wrinkle and form air bubbles during coating, which reduces the electroadhesive pressure. To minimize the influence of encapsulation and maximize the stiffness ratio,  $50\ \mu\text{m}$  TPU of 0.6 GPa Young's modulus (less than 8% of electrode film) is used as the vacuum envelope for the final sample.

#### IV. EXPERIMENTAL RESULTS

This section first introduces the experimental setup and protocols of the three-point bending test, which were then conducted to characterize the mechanical behaviors of HALJ in the fully composite and the following sliding regimes. The experimental results of HALJ with different numbers of layers under individual voltage driving, pure vacuum, and hybrid actuation were compared with theoretical predictions. The controllability and step response time of HALJ were exhibited by feedforward control. Finally, the coupling relationship between the negative pressure field and the electrical field of HALJ under hybrid actuation was experimentally characterized.

##### A. Experimental Setup and Protocols

The experimental setup (Fig. 9) shows that HALJ was mounted on two roller supporters. One end of HALJ was wired to the positive output of a high-voltage function generator (Model 615-3, Trek Inc.) and tubed with a vacuum regulator (IRV10, Anke Pneumatic Tech.), which was connected to a vacuum pump (VPC200,  $-84\ \text{kPa}$  Max., 50 L/min, Analysis Tech.). The other end was grounded by the generator and tubed to a miniature pressure sensor module (GZP6847A, Sencoch). The electroadhesive pressure and the negative pressure gradient were regulated by

the output voltage of the generator and the vacuum regulator, respectively. The pressure sensor recorded the negative pressure within the envelope on the other side, guaranteeing that uniform pressure was applied along the interfaces. Three-point bending tests were conducted to characterize the stiffness of two-layer and four-layer HALJ under different driving voltages, negative pressure gradients, and hybrid actuation of voltages and vacuuming combinations. During bending, an anvil of the testing machine (5966, 0.1 mN, Instron) applied a concentrated load on the midspan of HALJ at a velocity of 2 mm/min and stopped at the set deflection of 3 mm. Tests of specimens under each actuation were repeated three times.

##### B. Three-Point Bending

Fig. 10(a) is the three-point bending  $F$ - $w$  profiles of two-layer HALJ under individual voltage driving and pure vacuuming. It illustrates that, for two-layer HALJ, the electroadhesive pressure  $P_{EA}$  generated by 1 kV approximately equals 9 kPa, and therefore, the profile of that is close to the profile of 10 kPa vacuum pressure  $P_V$ . Since HALJ under 2 kV is two times 1 kV, the electroadhesive pressure increases to 36 kPa theoretically, as described in (1). Therefore, the profile of 2 kV is between the profiles of 30 and 40 kPa. It can be concluded that electroadhesive and vacuum pressures are competitive rivalries. Then, the hybrid actuation mechanism is explored. The profile of 2 kV ( $-36\ \text{kPa}$ ) and 10 kPa combination is slightly lower than the 50 kPa pure vacuum, but as the vacuum part of hybrid actuation rises, the 2 kV and 20 kPa combination are marginally higher than the 70 kPa pure vacuum [Fig. 10(b)]. Meanwhile, the 2 kV and 40 kPa combination profile is evidently higher than the 80 kPa pure vacuum [Fig. 10(c)]. To conclude, the equivalent hybrid pressure does not equal the separate superposition of electroadhesive and vacuum pressures for two-layer HALJ. This can be attributed to the air gap reduction between electrode films by the increase in the vacuum component, further promoting the electroadhesive pressure under the same voltage based on (1). Owing to the TPU encapsulation as a necessity to form an airtight chamber for vacuum actuation, the external forces at 3 mm deflection for 2 kV and 10, 20, and 40 kPa hybrid actuation combinations are 8.9%, 21.8%, and 36.3% higher than that of the 2 kV individual voltage driving case, respectively. To outperform HALJ with voltage breakdown and atmospheric pressure limitations, two-layer HALJ under 3 kV and 80 kPa combination, as shown in Fig. 10(c), reaches the equivalent pressure beyond 160 kPa based on (2), and is 23.2% higher in force than HALJ under individual vacuum actuation of 80 kPa.

The same as two layers, four-layer HALJ under individual voltage driving of 1 and 2 kV and pure vacuum of 10 and 40 kPa are characterized, as shown in Fig. 11(a). The equivalent electroadhesive pressures of 1 and 2 kV for four-layer HALJ are 9 and 40 kPa, respectively. The pressure increase of 2 kV can also be attributed to the reduced air gaps when the voltage is raised. However, unlike promoting EA through vacuum for two-layer HALJ, four-layer HALJ under hybrid actuation shows a superposition relationship between the electroadhesive and vacuum components, as revealed in Fig. 11(b). When four-layer

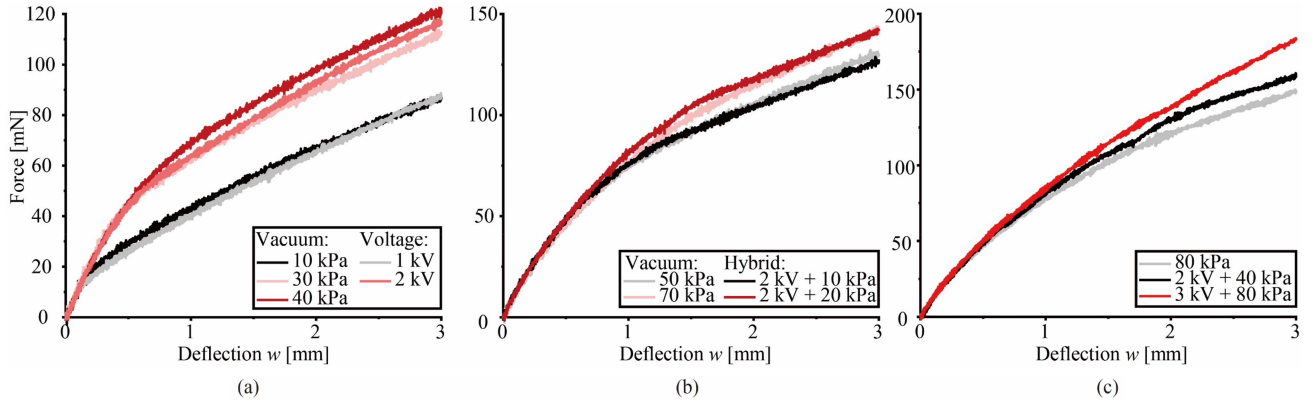


Fig. 10. Experimental results comparison of two-layer HALJ under (a) pure voltage driving of 1 and 2 kV and pure vacuum of 10, 30, and 40 kPa. (b) Hybrid actuation of 2 kV combined with 10 and 20 kPa, compared with individual vacuum of 50 and 70 kPa, respectively. (c) Comparison between 3 kV and 80 kPa combination, 2 kV and 40 kPa combination, and individual 80 kPa.

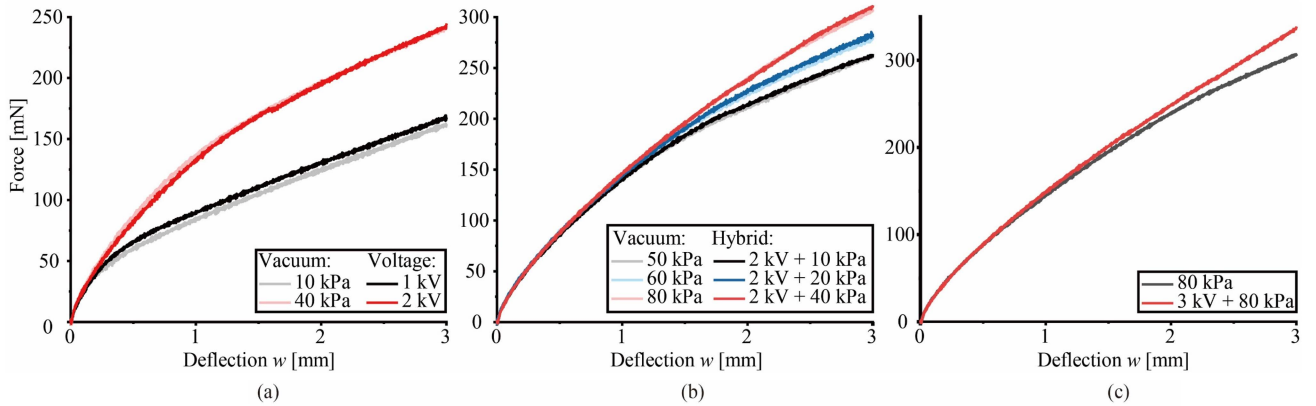


Fig. 11. Experimental results comparison of four-layer HALJ under (a) pure voltage driving of 1 and 2 kV and pure vacuum of 10 and 40 kPa. Hybrid actuation of (b) 2 kV combined with 10, 20, and 40 kPa, compared with individual vacuum of 50, 60, and 80 kPa, respectively. (c) Comparison between 3 kV and 80 kPa combination and 80 kPa.

HALJ actuated by 2 kV ( $-40$  kPa) combined with 10, 20, and 40 kPa, the profiles overlap with HALJ under 50, 60, and 80 kPa, respectively. Similar to the two-layer HALJ, the forces at 3 mm under those actuation combinations are 7.6%, 15.4%, and 27.4% higher than the 2 kV actuated one. Finally, as shown in Fig. 11(c), the four-layer HALJ under 3 kV and 80 kPa [ $-160$  kPa according to (2)] combination is 10.2% higher in force than that of four-layer HALJ under individual vacuum of 80 kPa.

Fig. 12(a) is the theoretical prediction and experimental results comparison of two-layer HALJ under no actuation, individual voltage driving of 3 kV, pure vacuum of 50 kPa, and hybrid actuation of 2 kV and 20 kPa combination, presenting high accuracy. HALJ with no actuation shows a simple linear mechanical behavior since its unjamming stiffness is constant, as (4) describes. Whether under individual or hybrid actuation, HALJ presents similar mechanical behaviors and experiences a shared linear regime with the highest jamming stiffnesses, followed by the nonlinear regime with stiffness variation, as (5) predicts. As shown in Fig. 12(b), NA of the two-layer HALJ actuated by a higher equivalent actuation pressure withstands at

TABLE III  
CONSTANT PARAMETERS AND SOURCE

Parameters	Source	Value
$E_t$ (GPa)	Datasheet	0.707
$E_e$ (GPa)	Measurement	8.747
$k_c$	Calculation	0.727
$B_2$ (50 kPa)	Empirical [24]	1.0004
$B_2$ (2 kV+20 kPa)	Empirical [24]	1.0031
$B_2$ (3 kV)	Empirical [24]	1.0023
$B_4$ (All actuation)	Trial	1.0010

the value of 1 with a larger deflection, meaning a longer linear regime (prolonging the yield points, marked with solid circles), as predicted by Fig. 6(f). Then, it moves slower to the value of zero, which means a slower stiffness variation, as described by (5) and (8). Fig. 12(c) (red dots) compares the theoretical and acquired force at the set deflection of 3 mm for two-layer HALJ under individual and hybrid actuation. The value of  $B_2$  for different actuation methods (Table III) are all close to the value of 1, illustrating that the two-layer HALJ in the fully sliding state

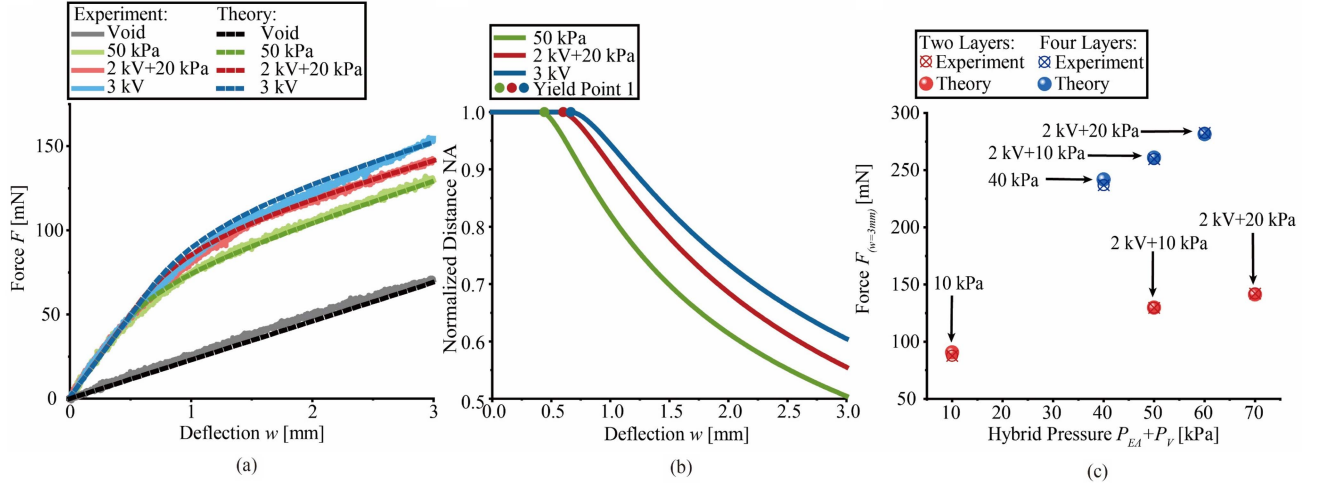


Fig. 12. Theoretical prediction and experimental validation. (a) Force-deflection plot of two-layer HALJ under pure voltage driving, pure vacuum, and hybrid actuation. (b) NA movement under the corresponding actuation. (c) External force prediction and validation at the end of bending for HALJ with different numbers of layers under different actuation. Standard deviations: 0.9 mN for two layers, 1.3 mN for four layers, and 1.1 mN for both individual and hybrid actuation.

TABLE IV  
ANALYTICAL SOLUTIONS FOR TWO-LAYER HALJ

Solution	$A_{(2,1)}$	$A_{(2,2)}$	$A_{(2,3)}$	$C_2$
Actuation				
50 kPa	-0.1399	1.0176	0.0004	-0.0567
2 kV and 20 kPa	-0.2551	1.3265	0.0026	-0.1661
3 kV	-0.3052	1.3886	0.0018	-0.1415

can be regarded as that in its unjammed state. The analytical solutions of  $NA(w)$  for two-layer HALJ are listed in Table IV.

To further validate the proposed theoretical model, a two-layer HALJ at 0.5 mm deflection successfully tracks a sinusoidal stiffness signal with feedforward control in Fig. 13(a). The good controllability can be enhanced with other closed-loop control strategies for practical applications in future work. Besides stiffnesses, the response time, defined as the rise/fall time in the step response, is investigated. It only took 5 ms for HALJ to transit between the soft and rigid states under EA actuation, as shown in Fig. 13(b). However, on the left of Fig. 13(c), the stiffening speed for vacuum actuation is 285 times slower than EA. Due to the flow rate limitation, the softening process on the right is 1519 times slower than the de-EA process. It can be accelerated through active air pumping.

As discussed in the Appendix, since encapsulation is not considered for the outer layers in the four-layer HALJ jamming model, it might be responsible for the possible discrepancies between theoretical and experimental results. To reduce the anomaly, the corresponding stiffness component  $K_1$  is corrected by a constant coefficient  $k_c$ , and thus, the governing (A9) becomes

$$F(w) = K_{U(4)}w + k_c K_1 NA_1^2(w)w + K_2 NA_2^2(w)w. \quad (17)$$

After correction, the model is robust enough to predict four-layer HALJ under different actuations, as shown in Fig. 14(a).

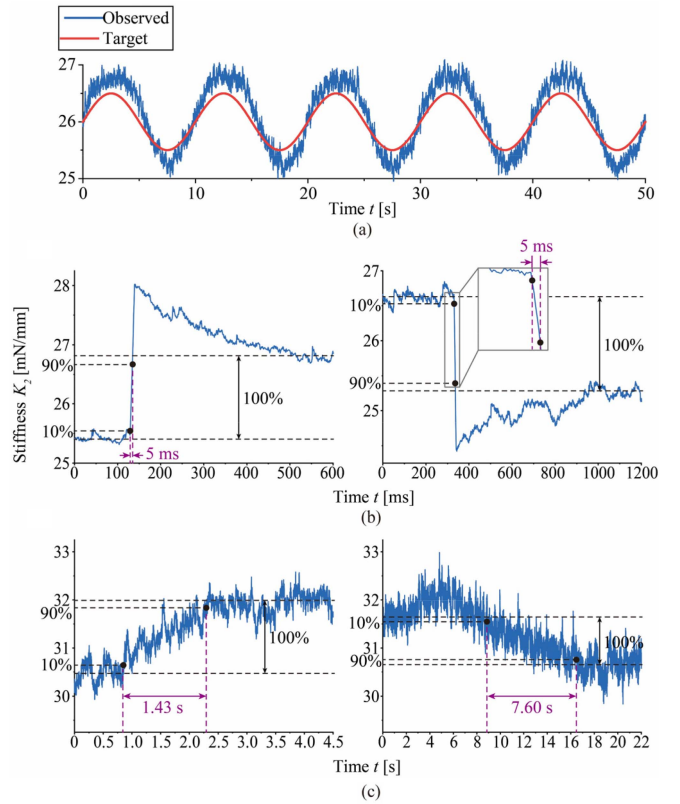


Fig. 13. Feedforward control of a two-layer HALJ to track (a) sinusoidal stiffness signals. The stiffness step responses of HALJ under (b) EA and (c) vacuum actuation are illustrated.

Similar to two layers, the corresponding deflection of the linear regime increases with actuation pressure [enlarged inset of Fig. 14(b)]. Although the external force of four-layer HALJ [blue dots in Fig. 12(c)] is larger than two-layer HALJ under the same equivalent actuation pressure, the linear regime deflections of

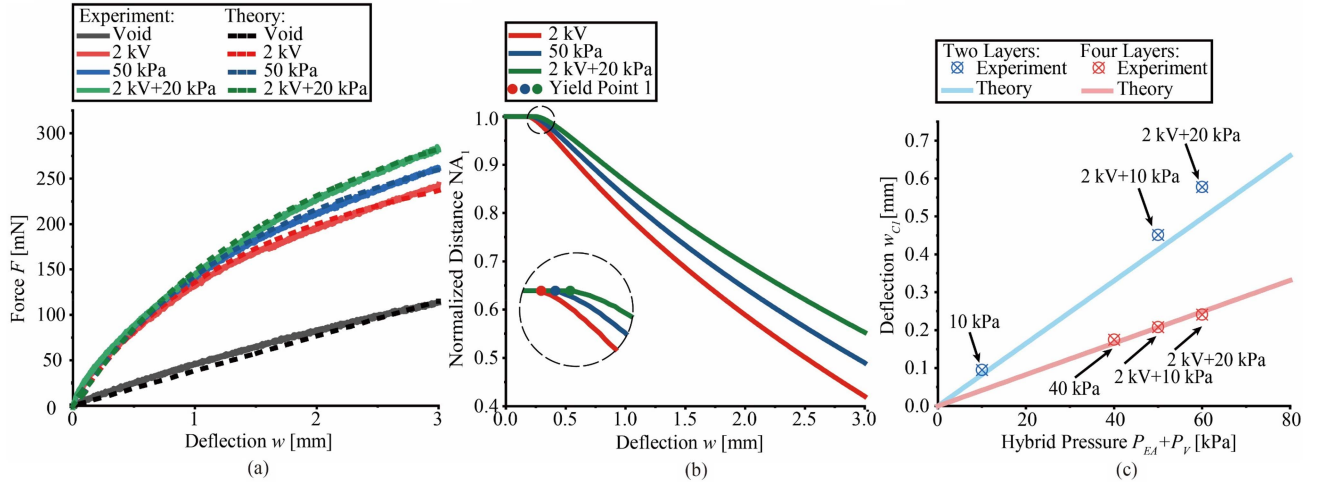


Fig. 14. Theoretical prediction and experimental validation. (a) Force-deflection plot of four-layer HALJ under individual voltage driving, individual vacuum, and hybrid actuation. (b) NA movement under the corresponding actuation. The enlarged inset shows a small increase in the linear regime. (c) Corresponding deflections at yield point 1 for HALJ with different numbers of layers under different actuation. Standard deviations: 0.02 mm for two layers, 0.002 mm for four layers, 0.005 mm for individual actuation, and 0.01 mm for hybrid actuation.

TABLE V  
ANALYTICAL SOLUTIONS FOR FOUR-LAYER HALJ

Solution	$NA_1(w)$				$NA_2(w)$			
	$A_{(4,1)}$	$A_{(4,2)}$	$A_{(4,3)}$	$C_{(4,1)}$	$A_{(4,4)}$	$A_{(4,5)}$	$A_{(4,6)}$	$C_{(4,2)}$
2 kV	-0.0011	-0.0807	-0.5637	1.4436	-12982.6697	13534.6923	1167.9662	-7502.9354
50 kPa	-0.0013	-0.0887	-0.5227	1.4466	-16365.2515	14621.2539	1081.2949	-7503.3682
2 kV and 20 kPa	-0.0015	-0.0990	-0.4865	1.4528	-20520.4211	15767.8583	1002.8985	-7504.2395

four-layer HALJ are much smaller than that of two-layer HALJ, as profiled in Fig. 14(c) and validated by the left part of Fig. 6(f). However, the conclusion that a higher actuation pressure results in a slower stiffness variation is still valid for four-layer HALJ, as shown in Fig. 14(b). The correction coefficient  $k_c$ , value of  $B_4$ , and other constant parameters used in the four-layer model are listed in Table III. The analytical solutions of  $NA_1(w)$  and  $NA_2(w)$  for four layers are in Table V. No analytical solutions with physical meanings were found for the situation where interlayer sliding first happens at the other interface in this model (see the Appendix). To evaluate and compare the agreement between theoretical and experimental results in different force scales, the root-mean-square error is calculated as follows:

$$e_{rms} = \frac{\sqrt{\frac{1}{N} \sum_1^N (F_{theo} - F_{exp})^2}}{\max(F_{theo})} \times 100\%. \quad (18)$$

The resultant values of  $e_{rms}$  are  $1.82 \pm 0.54\%$  and  $1.65 \pm 0.06\%$  for two-layer and four-layer HALJ under different actuation methods, respectively, presenting excellent and comparable agreement for HALJ with different number of layers. Therefore, the external force at arbitrary points during bending can be calculated with high accuracy through the analytical model with explicit solutions. Besides accurate theoretical predictions, small average force standard deviations (0.9 mN for two layers, 1.3 mN for four layers, and 1.1 mN for both individual

and hybrid actuation) exhibit good experimental repetitions of three times trials of HALJ under each actuation.

Similar to Fig. 10(b) and (c), where force promotion is observed, Fig. 14(c) again exhibits the enhancement in deflections of two-layer HALJ when the vacuum component increases while four-layer HALJ conforms to a linear relationship. As discussed, a possible explanation is that the air gap is reduced by vacuum actuation, and thus, EA is further enhanced accordingly based on (1). To prove this assumption, the coupling relationship between electrical and negative pressure fields should be analyzed by evaluating the air gap between electrode films.

### C. Air Gaps Reduction

The air gap between electrode films is affected by electroadhesive pressure and vacuum pressure in different mechanisms. The contacting interface for a two-layer structure can be modeled as a mass ( $m$ )-spring ( $k$ )-damper ( $c$ ) system, as shown in Fig. 15(a). To quantitatively analyze the air gap variation, the leakage current  $I$  was measured by an electrometer (Model 6514, Keithley Instruments) when HALJ was charged with different voltages [Fig. 15(b)]. The accumulated electric charge on electrode films within the charging process is calculated as follows:

$$Q = \int Idt = UC \quad (19)$$

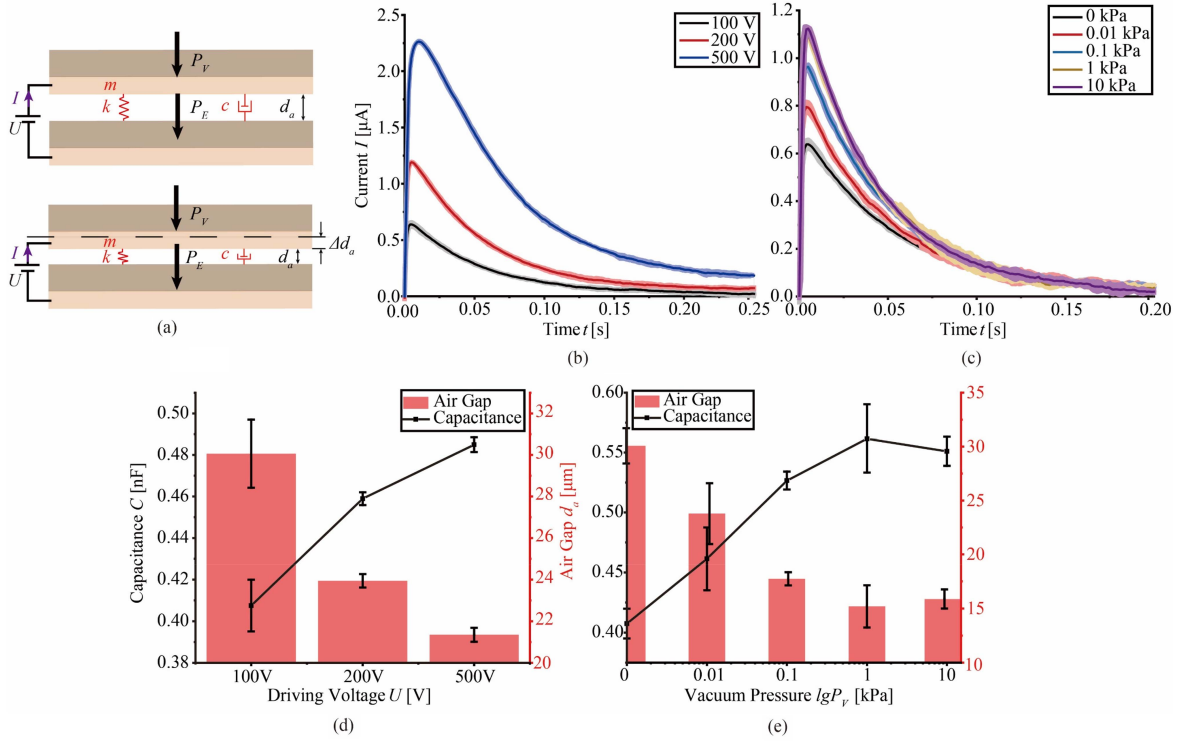


Fig. 15. Experimental results of the relationship between air gaps and the coupled electrical and negative pressure fields. (a) Mass-spring-damper modeling of the air gap at the contact interface. Measured current plot of two-layer HALJ under (b) different driving voltages and (c) different negative pressure gradients with a fixed voltage of 100 V. (d) and (e) Corresponding calculated capacitances and air gap thicknesses.

where  $C$  is the capacitance of two-layer HALJ. Therefore, the air gap is obtained

$$d_a = \varepsilon_0 \left( \frac{A}{C} - \frac{d}{\varepsilon_0 \varepsilon_r} \right) \quad (20)$$

where  $A = bL$  is the effective EA area between electrode films. For this second-order system

$$m \ddot{\Delta d}_a + c \dot{\Delta d}_a + k \Delta d_a = P_{EA/V} \quad (21)$$

where  $m$ ,  $c$ , and  $k$  are the mass, damping, and spring constants, respectively, the electroadhesive pressure induced by a step voltage input reduces the air gap and further enlarges the pressure according to (1) until systematic stabilization. As calculated in Fig. 15(d), the air gap becomes smaller with a larger voltage input, while the capacitance shows the contrary according to (20). The average values of the air gap are 30, 24, and 21  $\mu$ m for two-layer HALJ under 100, 200, and 500 V, respectively.

Regarding vacuum actuation, different negative pressure gradients were applied inside the vacuum chamber. Meanwhile, the corresponding current of HALJ under 100 V was recorded, as plotted in Fig. 15(c). Besides the similar air gap reduction process as the voltage actuation mentioned earlier, the vacuum removes air molecules from the chamber and, thus, lowers the system parameters of spring constant  $k$  and damping constant  $c$ , accelerating this process in Fig. 15(e). However, the system parameters become steady when the number of air molecules

decreases to a certain extent, e.g., 1 and 10 kPa in this case. Hence, the calculated air gap remains almost unchanged. The average values of the air gap are 30, 24, 18, 15, and 15  $\mu$ m for two-layer HALJ under 0, 0.01, 0.1, 1, and 10 kPa, respectively, when supplied with 100 V.

#### D. Breakdown Voltage

Besides air gap reduction, applied vacuum pressure also affects the breakdown voltage of HALJ based on Paschen's law

$$U_b = \frac{B \Delta P d_a}{\ln(\Delta P d_a) + K} \quad (22)$$

where  $\Delta P = P_a - P_V$  is the pressure inside the vacuum chamber, and  $B$  and  $K$  are constant parameters related to air [32]. The breakdown voltage  $U_b$  is the maximum voltage that can be applied on HALJ to fail EA. Breakdown requires moving electrons from neutral gas, air, in this case, through impact ionization, which largely depends on collision behaviors. Physically, a high value of  $\Delta P d_a$  in (22) represents a great possibility of collision between air molecules and electrons emitted from the cathode. As depicted in Fig. 16(a), for a relatively high density of air molecules before vacuuming, electrons increase exponentially during the ionization process to induce an electron avalanche. Thus, a lower voltage can trigger this process. With subatmospheric pressure applied, the mean free path of electrons becomes longer under the condition of a smaller  $\Delta P d_a$ . Namely, collisionality between a smaller amount of air molecules and

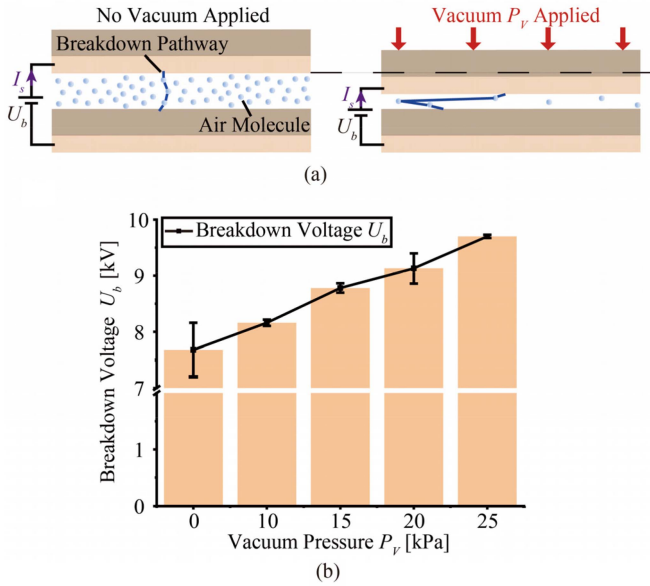


Fig. 16. Relationship between vacuum pressure and breakdown voltage. (a) Breakdown pathways of two-layer HALJ before and after vacuuming. (b) Experimental results of breakdown voltage of HALJ under different negative pressures.

electrons traveling through a reduced air gap is low. Therefore, a larger voltage (electrical energy) is required to create enough ions to achieve breakdown when fewer collisions happen [33]. This conclusion is validated by the experimental results in Fig. 16(b), where a 23% average increase in breakdown voltage for a two-layer HALJ under 25 kPa is found, compared with no vacuum applied. Breakdown voltages of HALJ vacuumed by 30 kPa and beyond surpass the maximum range of the dc amplifier used in this work (10 kV). Hence, HALJ, under greater vacuum pressure, can be applied with a larger driving voltage to augment its performance further.

## V. CONCLUSION

HALJ for VS was first designed and fabricated. Then, a multilayer model was built by considering the influence of encapsulation and analyzing sliding behaviors between interfaces. For the multiparameter inputs model, materials, geometries, and actuation were comprehensively quantitatively analyzed to improve the stiffness-related and force-related performance when designing the HALJ prototype. The analytical solutions were proven to highly agree with the experimental results of HALJ with different layers under individual/hybrid actuation. Feedforward control presented HALJ to track target stiffness signals and showed a fast step response. The proposed hybrid actuation mechanism surpassed the atmosphere limitation and increased the breakdown voltage.

Future work will focus on medical applications. For instance, HALJ can combine with an extracorporeal magnetic anchoring system [19] and surgical instruments to conduct grasp and adjustment procedures for surgical retraction in clinical practice. Besides retraction, HALJ can be employed as a force output platform to enhance the capabilities of end effectors on

endoscopes across a range of MIS, such as transluminal and transoral surgeries. Upon reaching the surgical site, the rapid and adaptable stiffness variation facilitates various continuous surgical manipulations on diverse tissue types with appropriate manipulative forces.

## APPENDIX

### A. Four Layers – Linear Model

A four-layer HALJ is consistent in structure with the two-layer HALJ but with four electrode films inside the TPU envelope. Namely, the four-layer HALJ can be regarded as two equivalent layers at the top and the bottom and two layers of electrode films at the central. Therefore, the unjamming stiffness  $K_{U(4)}$  for four layers also conforms to the superposition relationship and equals the sum of the stiffnesses of two equivalent layers and two electrode films

$$K_{U(4)} = 2 \frac{48E_e I_e}{l^3} + 2 \frac{48E_c I_c}{l^3}. \quad (\text{A1})$$

The constant before  $48E_e I_e / l^3$  in (A1) is the counted number of layers of electrode films. Hence, the jamming stiffness  $K_{J(4)}$  consists of three parts: the unjamming stiffness, the jamming stiffnesses from the equivalent layers, and the electrode films

$$K_{J(4)} = K_{U(4)} + 2 \frac{48E_e A_e}{l^3} \left( h_e + \frac{h_e}{2} \right)^2 + 2 \frac{48E_e A_e}{l^3} \left( \frac{h_e}{2} \right)^2. \quad (\text{A2})$$

Equation (A2) is the maximum value of jamming stiffness when the variable for the equivalent layer  $S_1/2 = 3h_e/2$  and  $S_2/2 = h_e/2$  for the electrode film, so the ratio of stiffness  $R_{(4)}$  is maximized in the linear region. Noted that unlike (5),  $E_e A_e$  is used in the second term of (A2) instead of  $E_c A_c$ , several considerations are accountable.

Though electroadhesive and negative pressures are characterized as equal components in (2) for providing interlayer attachment, the adhesion mechanisms are different. For two-layer HALJ, TPU films are involved in structural jamming when the negative pressure component is effective, such as direct vacuuming or hybrid actuation. For EA, the high voltage-induced ( $-kV$ ) opposite charges on the TPU film surface also result in interlayer adhesion to some extent. Thus, both TPU encapsulation and electrode films are considered engaging in jamming for the two-layer case under any actuation method, as described in (5). On the contrary, the TPU film influence is neglected in the four-layer jamming model, as described in (A2). As the number of electrode films increases, TPU films play a much less significant role in jamming stiffness by considering the fact that increased contacting interfaces in the layered structure complicate the adhesion environment and thus weaken the inductive EA between TPU films and electrode films. Similar to EA, although the tubing effect on HALJ stiffness is minimized with small-diameter TPU tubes, its existence deteriorates the vacuum environment inside the TPU envelope as the number of layers of electrode films and the contacting interfaces increase.

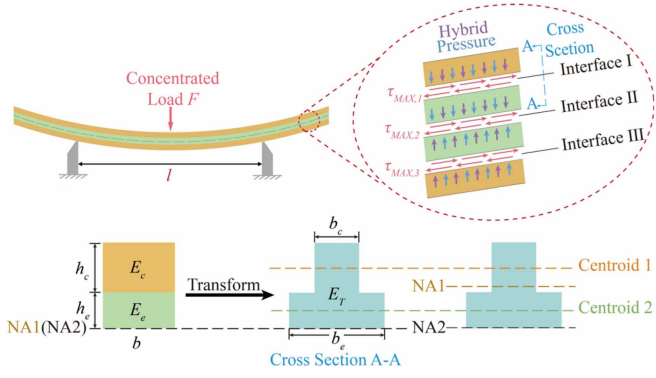


Fig. 17. Force diagram of a four-layer HALJ, including the NA1 movement of the transformed equivalent layer of the top half structure at yield point 2.

Hence, TPU layers are not considered in the jamming model for the four-layer situation but still affect the unjamming stiffness through Young's modulus and thickness, as described in (A1).

### B. Four Layers – Nonlinear Model

As shown at the top of Fig. 17, three interfaces remain to be analyzed for a four-layer HALJ. Sliding occurs chronologically along these interfaces as the external force rises but is regarded to happen simultaneously at Interface I and III due to structural symmetry. Hence, only Interface I and Interface II are discussed here. An assumption is that the sliding at Interface I happens before that at Interface II. The shear stresses at these interfaces need to be compared to validate this assumption. Before that, the equivalent layer and electrode film with different moduli are transformed into a reversed T-shaped beam with different widths, as shown at the bottom of Fig. 17. The modulus and widths after transformation are calculated as follows:

$$E_T = E_e \frac{2h_e}{h_e + h_c} + E_t \frac{h_t}{h_e + h_c} \quad (\text{A3})$$

and

$$\begin{cases} b_e = \frac{E_e}{E_T} b \\ b_c = \frac{E_c}{E_T} b \end{cases} \quad (\text{A4})$$

The shear stress at Interface I and Interface II are then derived as follows:

$$\begin{cases} \tau_{MAX,1} = \frac{F_{C(4,1)}}{2} \frac{S_{z1}}{I_{J(4,1)} b_c} \\ \tau_{MAX,2} = \frac{F_{C(4,2)}}{2} \frac{S_{z2}}{I_{J(4,2)} b_e} \end{cases} \quad (\text{A5})$$

where

$$\begin{cases} S_{z1} = b_c h_c (h_e + \frac{h_c}{2}) \\ S_{z2} = b_e h_e \frac{h_e}{2} + b_c h_c (h_e + \frac{h_c}{2}) NA_1(w_{C(4,2)}) \end{cases} \quad (\text{A6})$$

are the first moment of the portion of the cross-section located above the point of interest with respect to the corresponding NA,

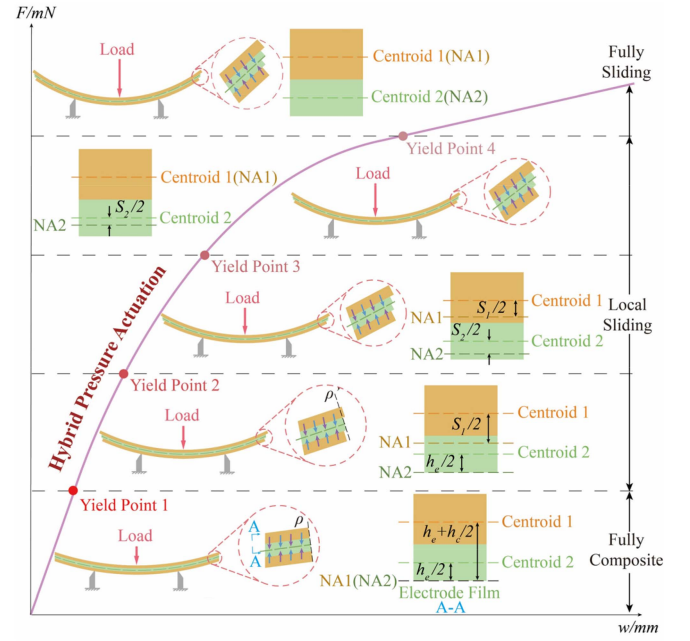


Fig. 18. Schematic of mechanical behaviors for a four-layer HALJ under a three-point bending test, where three regimes, fully composite, local sliding, and fully sliding along contact interfaces, chronologically happen. HALJ in fully composite remains the highest stiffness, where NA1 and NA2 overlap at Interface II. After yield point 1, the first sliding occurs at Interface I, resulting in NA1 movement to Centroid 1 while NA2 remains still at its initial position, thus, stiffness decreases. As the external load increases, the second sliding occurs at Interface II, where the movement of NA2 to Centroid 2 commences (yield point 2) while NA1 continues approaching Centroid 1. Finally, NA1 overlaps with Centroid 1 (yield point 3), followed by the coincidence of NA2 and Centroid 2, where the fully sliding regime starts (yield point 4).

and

$$\begin{cases} I_{J(4,1)} = \frac{b_e (2h_e)^3}{12} + 2 \frac{b_c h_c^3}{12} + 2b_c h_c (h_e + \frac{h_c}{2})^2 \\ I_{J(4,2)} = \frac{b_e (2h_e)^3}{12} + 2 \frac{b_c h_c^3}{12} + 2b_c h_c (h_e + \frac{h_c}{2})^2 NA_1^2(w_{C(4,2)}) \end{cases} \quad (\text{A7})$$

are the corresponding moment of inertia  $I_{J(4,1)}$  and  $I_{J(4,2)}$  at yield point 1 and yield point 2, respectively.  $NA_1(w_{C(4,2)})$  represents the unknown normalized distance between NA1 and Centroid 1 of the equivalent layer at the corresponding deflection  $w_{C(4,2)}$  of yield point 2, as shown at the most right of Fig. 17. Based on (6), the maximum shear stress  $\tau_{MAX,1}$  at yield point 1 is the same as the maximum shear stress  $\tau_{MAX,2}$  at yield point 2 for a given hybrid pressure. Therefore, the ratio of critical forces at yield points 1 and 2 can be obtained from (A5)

$$\frac{F_{C(4,2)}}{F_{C(4,1)}} = \frac{S_{z1} I_{J(4,2)} b_e}{S_{z2} I_{J(4,1)} b_c} \quad (\text{A8})$$

For  $NA_1(w_{C(4,2)}) \in [1, 0]$ , the calculated ratio of (A8) ranges from 1.20 to 0.80 accordingly. When  $F_{C(4,2)} > F_{C(4,1)}$  (ratio of critical forces  $> 1$ ), the assumption of the first sliding occurring at Interface I is valid. Thus, the following analysis is based on this assumption. The case of  $F_{C(4,2)} < F_{C(4,1)}$  will be discussed and compared with the former case later.

As illustrated in Fig. 18, a four-layer HALJ under hybrid actuation is considered fully composite at the beginning of bending,



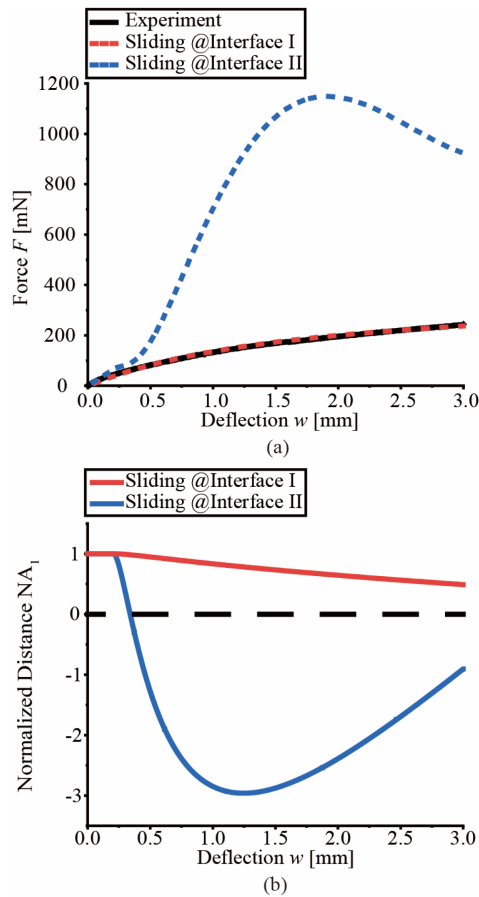


Fig. 19. Comparison of (a) forces and (b) NA movement between the two sliding assumptions for four-layer HALJ under 50 kPa.

case. It is reasonable that the blue dashed line shows a much higher profile in force because the third term is only 1/9 of the second term of the jamming stiffness in (A2) and decreases first once entering the nonlinear regime if assumption 2 is valid, resulting in a higher loading force in (A9). However, the force decrease after 2 mm deflection cannot be explained. On the contrary, based on the assumption of the first sliding occurrence at Interface I (assumption 1), the resultant profile successfully predicts the variable jamming stiffness and, thus, accurately characterizes the mechanical behaviors as expected in Fig. 19(a). Accordingly, Fig. 19(b) compares the NA movement based on the two assumptions. Both present decreases at the beginning of sliding, but assumption 2 quickly surpasses the reference line afterward, which is unacceptable because any negative value of the normalized distance  $NA(w)$  does not have physical meaning in this model. Then, the following increase in the negative zone is unexplainable. Finally, it does not converge to zero and, therefore, fails to yield to the boundary conditions in (A14). Unlike assumption 2, assumption 1 in Fig. 19(b) shows a reasonable continuous decrease within the physical range of [1,0], representing NA approaches its Centroid slowly and finally overlaps when converging to zero.

## REFERENCES

- [1] A. Shiva et al., "Tendon-based stiffening for a pneumatically actuated soft manipulator," *IEEE Robot. Automat. Lett.*, vol. 1, no. 2, pp. 632–637, Jul. 2016, doi: [10.1109/Ira.2016.2523120](https://doi.org/10.1109/Ira.2016.2523120).
- [2] K. Suzumori, S. Wakimoto, K. Miyoshi, and K. Iwata, "Long bending rubber mechanism combined contracting and extending fluidic actuators," in *Proc. IEEE/RSJ Int. Conf. Intell. Robots Syst.*, Nov. 2013, pp. 4454–4459, doi: [10.1109/iros.2013.6696996](https://doi.org/10.1109/iros.2013.6696996).
- [3] Y. Zhang et al., "Fast-response, stiffness-tunable soft actuator by hybrid multimaterial 3D printing," *Adv. Funct. Mater.*, vol. 29, no. 15, Apr. 2019, Art. no. 1806698, doi: [10.1002/adfm.201806698](https://doi.org/10.1002/adfm.201806698).
- [4] W. Shan, T. Lu, and C. Majidi, "Soft-matter composites with electrically tunable elastic rigidity," *Smart Mater. Struct.*, vol. 22, no. 8, Jul. 2013, Art. no. 085005, doi: [10.1088/0964-1726/22/8/085005](https://doi.org/10.1088/0964-1726/22/8/085005).
- [5] J. Lussi et al., "A submillimeter continuous variable stiffness catheter for compliance control," *Adv. Sci.*, vol. 8, no. 18, Jul. 2021, Art. no. 2101290, doi: [10.1002/advs.202101290](https://doi.org/10.1002/advs.202101290).
- [6] A. Arezzo et al., "Total mesorectal excision using a soft and flexible robotic arm: A feasibility study in cadaver models," *Surg. Endoscopy*, vol. 31, no. 1, pp. 264–273, Jun. 2016, doi: [10.1007/s00464-016-4967-x](https://doi.org/10.1007/s00464-016-4967-x).
- [7] N. G. Cheng et al., "Design and analysis of a robust, low-cost, highly articulated manipulator enabled by jamming of granular media," in *Proc. IEEE Int. Conf. Robot. Automat.*, May 2012, pp. 4328–4333, doi: [10.1109/icra.2012.6225373](https://doi.org/10.1109/icra.2012.6225373).
- [8] A. Cavallo, M. Brancadoro, S. Tognarelli, and A. Menciassi, "A soft retraction system for surgery based on ferromagnetic materials and granular jamming," *Soft Robot.*, vol. 6, no. 2, pp. 161–173, Apr. 2019, doi: [10.1089/soro.2018.0014](https://doi.org/10.1089/soro.2018.0014).
- [9] A. Jiang et al., "Robotic granular jamming: Does the membrane matter?," *Soft Robot.*, vol. 1, no. 3, pp. 192–201, Sep. 2014, doi: [10.1089/soro.2014.0002](https://doi.org/10.1089/soro.2014.0002).
- [10] Y. Li, Y. Chen, Y. Yang, and Y. Wei, "Passive particle jamming and its stiffening of soft robotic grippers," *IEEE Trans. Robot.*, vol. 33, no. 2, pp. 446–455, Apr. 2017, doi: [10.1109/tro.2016.2636899](https://doi.org/10.1109/tro.2016.2636899).
- [11] M. Brancadoro, M. Manti, S. Tognarelli, and M. Cianchetti, "Fiber jamming transition as a stiffening mechanism for soft robotics," *Soft Robot.*, vol. 7, pp. 663–674, Apr. 2020, doi: [10.1089/soro.2019.0034](https://doi.org/10.1089/soro.2019.0034).
- [12] L. Arleo, L. Lorenzon, and M. Cianchetti, "Variable stiffness linear actuator based on differential drive fiber jamming," *IEEE Trans. Robot.*, vol. 39, no. 6, pp. 4429–4442, Dec. 2023, doi: [10.1109/TRO.2023.3236941](https://doi.org/10.1109/TRO.2023.3236941).
- [13] T. Miller-Jackson, Y. Sun, R. Natividad, and C. H. Yeow, "Tubular jamming: A variable stiffening method toward high-force applications with soft robotic components," *Soft Robot.*, vol. 6, no. 4, pp. 468–482, Aug. 2019, doi: [10.1089/soro.2018.0084](https://doi.org/10.1089/soro.2018.0084).
- [14] M. Henke and G. Gerlach, "On a high-potential variable-stiffness device," *Microsystem Technol.*, vol. 20, no. 4–5, pp. 599–606, Dec. 2013, doi: [10.1007/s00542-013-1995-5](https://doi.org/10.1007/s00542-013-1995-5).
- [15] Y. Zhou, L. M. Headings, and M. J. Dapino, "Discrete layer jamming for safe co-robots," in *Proc. Int. Conf. Robot. Automat.*, May 2019, pp. 6124–6129, doi: [10.1109/icra.2019.8793908](https://doi.org/10.1109/icra.2019.8793908).
- [16] Y. S. Narang, J. J. Vlassak, and R. D. Howe, "Mechanically versatile soft machines through laminar jamming," *Adv. Funct. Mater.*, vol. 28, no. 17, Apr. 2018, Art. no. 1707136, doi: [10.1002/adfm.201707136](https://doi.org/10.1002/adfm.201707136).
- [17] Y. Narang, A. Degirmenci, J. J. Vlassak, and R. D. Howe, "Transforming the dynamic response of robotic structures and systems through laminar jamming," *IEEE Robot. Automat. Lett.*, vol. 3, no. 2, pp. 688–695, Apr. 2018, doi: [10.1109/Ira.2017.2779802](https://doi.org/10.1109/Ira.2017.2779802).
- [18] Y. S. Narang, B. Aktaş, S. Ornellas, J. J. Vlassak, and R. D. Howe, "Lightweight highly tunable jamming-based composites," *Soft Robot.*, vol. 7, pp. 724–735, Apr. 2020, doi: [10.1089/soro.2019.0053](https://doi.org/10.1089/soro.2019.0053).
- [19] Y.-J. Kim, S. Cheng, S. Kim, and K. Iagnemma, "A novel layer jamming mechanism with tunable stiffness capability for minimally invasive surgery," *IEEE Trans. Robot.*, vol. 29, no. 4, pp. 1031–1042, Aug. 2013, doi: [10.1109/tro.2013.2256313](https://doi.org/10.1109/tro.2013.2256313).
- [20] I. Choi, N. Corson, L. Peiros, E. W. Hawkes, S. Keller, and S. Follmer, "A soft, controllable, high force density linear brake utilizing layer jamming," *IEEE Robot. Automat. Lett.*, vol. 3, no. 1, pp. 450–457, Jan. 2018, doi: [10.1109/Ira.2017.2761938](https://doi.org/10.1109/Ira.2017.2761938).
- [21] M. Ibrahim, L. Paternò, L. Ricotti, and A. Menciassi, "A layer jamming actuator for tunable stiffness and shape-changing devices," *Soft Robot.*, vol. 8, pp. 85–96, May 2020, doi: [10.1089/soro.2019.0182](https://doi.org/10.1089/soro.2019.0182).
- [22] F. Caruso, G. Mantriota, L. Afferrante, and G. Reina, "A theoretical model for multilayer jamming systems," *Mechanism Mach. Theory*, vol. 172, Jun. 2022, Art. no. 104788, doi: [10.1016/j.mechmachtheory.2022.104788](https://doi.org/10.1016/j.mechmachtheory.2022.104788).

- [23] F. Caruso, G. Mantriota, V. Moramarco, and G. Reina, "Layer jamming: Modeling and experimental validation," *Int. J. Mech. Sci.*, vol. 251, Aug. 2023, Art. no. 108325, doi: [10.1016/j.ijmecsci.2023.108325](https://doi.org/10.1016/j.ijmecsci.2023.108325).
- [24] C. Chen, D. Fan, H. Ren, and H. Wang, "Comprehensive model of laminar jamming variable stiffness driven by electrostatic adhesion," *IEEE/ASME Trans. Mechatron.*, vol. 29, no. 3, pp. 1670–1679, Jun. 2024, doi: [10.1109/TMECH.2023.3319650](https://doi.org/10.1109/TMECH.2023.3319650).
- [25] T. Wang, J. Zhang, Y. Li, J. Hong, and M. Y. Wang, "Electrostatic layer jamming variable stiffness for soft robotics," *IEEE/ASME Trans. Mechatron.*, vol. 24, no. 2, pp. 424–433, Apr. 2019, doi: [10.1109/tmech.2019.2893480](https://doi.org/10.1109/tmech.2019.2893480).
- [26] H. Imamura, K. Kadooka, and M. Taya, "A variable stiffness dielectric elastomer actuator based on electrostatic chucking," *Soft Matter*, vol. 13, no. 18, pp. 3440–3448, 2017, doi: [10.1039/c7sm00546f](https://doi.org/10.1039/c7sm00546f).
- [27] Q. Xiong et al., "So-EAGlove: VR haptic glove rendering softness sensation with force-tunable electrostatic adhesive brakes," *IEEE Trans. Robot.*, vol. 38, no. 6, pp. 3450–3462, Dec. 2022, doi: [10.1109/tro.2022.3172498](https://doi.org/10.1109/tro.2022.3172498).
- [28] G. Xie et al., "Strong reliable electrostatic actuation based on self-clearing using a thin conductive layer," *Soft Robot.*, vol. 10, no. 4, pp. 673–859, Aug. 2023, doi: [10.1089/soro.2022.0132](https://doi.org/10.1089/soro.2022.0132).
- [29] D. Wei et al., "Electrostatic adhesion clutch with superhigh force density achieved by MXene-poly(vinylidene fluoride-trifluoroethylene-chlorotrifluoroethylene) composites," *Soft Robot.*, vol. 10, no. 3, pp. 482–492, Jun. 2023, doi: [10.1089/soro.2022.0013](https://doi.org/10.1089/soro.2022.0013).
- [30] Y. Sun et al., "Electrostatic layer jamming variable stiffness enhanced by giant electrorheological fluid," *IEEE/ASME Trans. Mechatron.*, vol. 29, no. 1, pp. 324–334, Feb. 2024, doi: [10.1109/tmech.2023.3275961](https://doi.org/10.1109/tmech.2023.3275961).
- [31] W. Yu, J. Liu, X. Li, Z. Yu, and H. Yuan, "A novel hybrid variable stiffness mechanism: Synergistic integration of layer jamming and shape memory polymer," *IEEE Robot. Automat. Lett.*, vol. 9, no. 3, pp. 2734–2741, Jan. 2024, doi: [10.1109/lra.2024.3357035](https://doi.org/10.1109/lra.2024.3357035).
- [32] E. Husain and R. S. Nema, "Analysis of Paschen curves for air, N2 and SF6 using the Townsend breakdown equation," *IEEE Trans. Elect. Insul.*, vol. EI-17, no. 4, pp. 350–353, Aug. 1982, doi: [10.1109/tei.1982.298506](https://doi.org/10.1109/tei.1982.298506).
- [33] D. B. Go and A. Venkatraman, "Microscale gas breakdown: Ion-enhanced field emission and the modified Paschen's curve," *J. Phys. D: Appl. Phys.*, vol. 47, no. 50, Nov. 2014, Art. no. 503001, doi: [10.1088/0022-3727/47/50/503001](https://doi.org/10.1088/0022-3727/47/50/503001).



**Cheng Chen** received the B.S. degree in mechanical engineering from the University of Electronic Science and Technology of China, Chengdu, China, in 2019, and the Ph.D. degree in biomedical engineering from the National University of Singapore, Singapore, in 2024.

He is currently a Visiting Scholar with the Department of Mechanical and Energy Engineering, Southern University of Science and Technology, Shenzhen, China, and an Honorary Postdoctoral Fellow with the Department of Electronic Engineering, The Chinese

University of Hong Kong, Hong Kong. His research interests include soft robotics and variable stiffness.



**Hongliang Ren** (Senior Member, IEEE) received the Ph.D. degree in electronic engineering (specialized in biomedical engineering) from The Chinese University of Hong Kong (CUHK), Hong Kong, in 2008.

He has navigated his academic journey through CUHK, Johns Hopkins University, Children's Hospital Boston, Harvard Medical School, Children's National Medical Center, USA, and National University of Singapore (NUS). He is currently a Professor with the Department of Electronic Engineering, CUHK. His research interests include biorobotics, intelligent control, medical mechatronics, soft continuum robots, soft sensors, and multi-sensory learning in medical robotics.



**Hongqiang Wang** (Senior Member, IEEE) received the B.S. and M.S. degrees in mechanical engineering from Xi'an Jiao Tong University, Xi'an, China, in 2008 and 2011, respectively, and the Ph.D. degree in precision mechanical engineering from Tokyo University, Tokyo, Japan, in 2015.

He is currently an Associate Professor with the Department of Mechanical and Energy Engineering, Southern University of Science and Technology, Shenzhen, China. His research interests include novel actuators, miniature robotics, new flexible actuators, soft robotics, and medical robotics.